Temporal evolution of ^{142}Nd signatures in SW Greenland from high precision MC-ICP-MS measurements

Eric Hasenstab-Dübeler [a,*], Jonas Tusch [a], J. Elis Hoffmann [b], Mario Fischer-Gödde [a], Kristoffer Szilas [c], Carsten Münker [a]

[a] *Institut für Geologie und Mineralogie, Universität zu Köln, Cologne, Germany*
[b] *Institut für Geologische Wissenschaften, Geochemie, Freie Universität Berlin, Berlin, Germany*
[c] *Department of Geosciences and Natural Resource Management, University of Copenhagen, Copenhagen, Denmark*

ARTICLE INFO

ABSTRACT

Measurements of ^{142}Nd isotope signatures in Archean rocks are a powerful tool to investigate the earliest silicate differentiation events on Earth. Here, we introduce a new analytical protocol that allows high precision radiogenic and mass-independent Nd isotope measurements by MC-ICP-MS. To validate our method, we have measured well-characterized ~3.72 to ~3.8 Ga samples from the Eoarchean Itsaq Gneiss Complex and associated supracrustal belts, as well as Mesoarchean greenstones and a Proterozoic dike in SW Greenland, including lithostratigraphic units that were previously analyzed for $^{142-143}$Nd isotope systematics, by both TIMS and MC-ICP-MS. Our μ^{142}Nd values for ~3.72 to ~3.8 Ga rocks from the Isua region range from +9.2 ± 2.6 to +13.2 ± 1.1 ppm and are in good agreement with previous studies. Using coupled ^{142,143}Nd/^{144}Nd isotope systematics from our data for ~3.8 Ga mafic-ultramafic successions from the Isua region, we can confirm previous age constraints on the earliest silicate differentiation events with differentiation age of $4.390^{+0.045}_{-0.060}$ Ga. Moreover, we can resolve a statistically significant decrease of ^{142}Nd/^{144}Nd isotope compositions in the ambient mantle of SW Greenland that already started to commence by Eoarchean time, between ~3.8 Ga (μ^{142}Nd = +13.0 ± 1.1) and ~ 3.72 Ga (μ^{142}Nd = +9.8 ± 1.0). Even lower but homogeneous μ^{142}Nd values of +3.8 ± 1.1 are found in ~3.4 Ga mantle-derived rocks from the Ameralik dike swarms. Our study reveals that ε^{143}Nd$_{(i)}$ and εHf$_{(i)}$ values of Isua rocks scatter more than it would be expected from a single stage differentiation event as implied from nearly uniform μ^{142}Nd values, suggesting that the previously described decoupling of Hf and Nd isotopes is not a primordial magma ocean signature. Instead, we conclude that some of second stage processes like younger mantle depletion events or recycling of subducted material affected the ^{147}Sm—^{143}Nd isotope systematics. The preservation of pristine whole-rock isochrons largely rules out a significant disturbance by younger alteration events. Based on isotope and trace element modelling, we argue that the temporal evolution of coupled ^{142,143}Nd/^{144}Nd isotope compositions in the ambient mantle beneath the Isua rocks is best explained by the progressive admixture of material to the Isua mantle source that must have had present-day-like μ^{142}Nd compositions. In contrast, Mesoarchean mafic rocks from the ~3.08 Ga Ivisaartoq greenstone belt and the 2.97 Ga inner Ameralik Fjord region as well as a 2.0 Ga Proterozoic dike within that region all have higher μ^{142}Nd values as would be expected from our simple replenishment model. This argues for reworking of older Isua crustal material that carried elevated μ^{142}Nd compositions.

1. Introduction

The long-lived ^{147}Sm—^{143}Nd isotope system has become a key analytical tool in geochronology and geochemistry issues. Its potential can be significantly increased when it is combined with the short-lived ^{146}Sm—^{142}Nd decay system (T$_{1/2}$ = 103 Ma (Friedman et al., 1966;

Meissner et al., 1987; Marks et al., 2014)) that was only active within the first few 100 Ma. Since Harper and Jacobsen (1992) reported the first anomalous ^{142}Nd/^{144}Nd compositions in Archean rocks (typically expressed in μ-notation, depicting the ppm deviation from a terrestrial reference material), this short-lived isotope system has been widely applied to numerous Archean terranes (e.g., Caro et al., 2003; Caro et al.,

2005; Boyet and Carlson, 2006; Rizo et al., 2012; Puchtel et al., 2016; Caro et al., 2017; Morino et al., 2017; Archer et al., 2019). When combined, coupled ^{147,146}Sm-^{143,142}Nd isotope systematics can yield valuable information about early geodynamic processes. Especially the Isua region in SW Greenland has drawn a particular interest in the scientific community, since this Archean remnant shows elevated ^{142}Nd/^{144}Nd compositions that were interpreted to reflect Hadean silicate differentiation (Harper and Jacobsen, 1992; Boyet et al., 2003; Caro et al., 2003; Caro et al., 2006; Bennett et al., 2007; Rizo et al., 2012). Anomalous ^{142}Nd/^{144}Nd isotope compositions are predominantly found in Paleo- to Eoarchean cratons (Boyet and Carlson, 2006; Caro et al., 2006; Rizo et al., 2011; Rizo et al., 2012; Rizo et al., 2016; Caro et al., 2017; Morino et al., 2017) and their broad disappearance after ~3.5 to ~3.0 Ga has been interpreted to reflect mantle homogenization processes (Boyet and Carlson, 2006; Caro et al., 2006; Bennett et al., 2007; Rizo et al., 2012; Saji et al., 2018; Schneider et al., 2018; Hyung and Jacobsen, 2020). However, with increasing analytical precision and higher numbers of rocks being investigated, anomalous ^{142}Nd/^{144}Nd isotope compositions have also been reported for Meso- and Neoarchean and even present-day rocks (Debaille et al., 2013; Rizo et al., 2013; Horan et al., 2018; Peters et al., 2018). Therefore, ^{142}Nd/^{144}Nd isotope studies can also provide information on the timing and efficiency of mantle homogenization processes. To better understand Archean mantle homogenization processes, rocks from SW Greenland provide an excellent opportunity as they comprise a variety of rocks with different crystallization ages (3.88–3.6 Ga in the Itsaq Gneiss Complex (IGC), including mantle rocks from associated greenstone remnants (Nutman and Friend, 2009; Amelin et al., 2011), ~3.2–3.5 Ga Ameralik dikes (Nutman et al., 2004; Rizo et al., 2012) and multiple younger ~3.1 to 2.8 Ga old Mesoarchean rocks from subduction-related terranes (Szilas, 2018).

Accurate and high precision isotope measurements are essential to resolve small ^{142}Nd isotope anomalies. In the past, thermal ionization mass spectrometry (TIMS) was almost exclusively preferred to conduct such high precision measurements, owing to comparatively small instrumentally induced mass fractionation effects. Although the vast majority of recent TIMS studies provided highly precise Nd isotope data (errors usually $\leq \pm 5$ ppm), the accuracy and reliability of TIMS protocols for ^{142}Nd measurement has often been debated, largely due to irreproducible mass fractionation effects. Reported problems included issues with static measurements (Brandon et al., 2009) reservoir mixing on the filament (Upadhyay et al., 2008) or changes in mass fractionation during acquisition steps (Garçon et al., 2018). All these issues call for alternative protocols to improve the analytical precision and accuracy of ^{142}Nd measurements. More recently, there has been an increasing number of multi-collector inductively coupled plasma mass spectrometry (MC ICP-MS) protocols that enabled high precision isotope measurements (e.g., ^{182}W or ^{142}Nd) with an analytical resolution power similar to that of TIMS analysis (e.g., Willbold, 2007; Saji et al., 2016; Saji et al., 2018; Budde et al., 2019; Tusch et al., 2019).

In this present study, we have developed a new MC ICP-MS protocol to determine mass-independent and radiogenic Nd isotope compositions at high precision and accuracy. We applied our newly developed analytical protocol to well characterized ~3.8 to ~3.7 Ga rocks from the IGC and associated greenstone belts, the ~3.3 to ~3.5 Ga Ameralik dikes and several terrestrial reference materials. Due to the high number of existing ^{142}Nd/^{144}Nd data on Isua rocks, these data allow an assessment of our new protocol in terms of accuracy and precision by cross referencing with previously published results (e.g., Caro et al., 2003; Boyet and Carlson, 2006; Caro et al., 2006; Bennett et al., 2007; Rizo et al., 2011; Saji et al., 2018). In addition, we have measured younger ~3.1 to ~2.0 Ga Mesoarchean rocks from subduction zone-related rocks from the Ivisaartoq supracrustal belt and the Ameralik Fjord region. These data are incorporated into the existing framework investigating the early differentiation history of Earth's mantle with the aim of better understanding the mechanisms that homogenized initially heterogeneous Eoarchean ^{142}Nd/^{144}Nd isotope compositions by the end of the Archean eon.

2. Geological background and sample description

Unlike many other Archean terranes that are usually of Paleoarchean age or younger, the Eoarchean 3.88–3.6 Ga IGC and associated greenstone belts allow insights into the earliest silicate differentiation processes preserved on Earth (Nutman and Friend, 2009). For supracrustal belts within the IGC, the Isua region has attracted increasing attention in the last decades, due to its good preservation (metamorphism often only up to amphibolite facies at locally little deformation), with some domains having only experienced little to no post-3.5 Ga strain (e.g., Moorbath et al., 1977; Friend et al., 1996; Nutman et al., 1999; Polat et al., 2002; Polat and Hofmann, 2003). Generally, the Isua Supracrustal Belt (ISB) can be divided into two formerly separate terranes, a northern ~3.7 Ga old terrane and a southern ~3.8 Ga old terrane (Nutman et al., 1997) that both show geochemical similarities to modern island arcs (Polat et al., 2002; Polat and Hofmann, 2003; Nutman and Friend, 2009). In the region south of the Isua greenstone belt (SOISB), the IGC contains a mixture of ~3.8 Ga felsic rocks, ultramafic pods and amphibolites that are preserved as enclaves in low strain domains (Friend et al., 1996; Nutman et al., 1999; Nutman et al., 2002; Crowley, 2003; van de Löcht et al., 2020) embedded in up to 3.88 Ga old TTG orthogneisses (Amelin et al., 2011) (Figs. 1 and Extended Data Fig. 1).

An interlayered <3.75 Ga mylonitized sedimentary unit within the ISB separates the northern ~3.7 Ga terrane from the older ~3.8 Ga southern terrane. Its deformation resulted from the juxtaposition of the northern and southern terrane between 3.69 and 3.66 Ga (Nutman et al., 1999; Nutman et al., 2007; Nutman et al., 2009) (Fig. 1). The ~3.7 Ga terrane can be subdivided into three sub-terranes that are associated with the occurrence of boninites, island arc tholeiites and intermediate to felsic schists (Polat et al., 2002; Polat and Hofmann, 2003; Nutman et al., 2009). Due to their strong geochemical similarities with modern analogues from subduction zone settings, the metavolcanic rocks were interpreted to have formed in a similar geodynamic setting (Polat et al., 2002; Polat and Hofmann, 2003; Nutman et al., 2007; Jenner et al., 2009; Hoffmann et al., 2010; Hoffmann et al., 2011b; Hoffmann et al., 2012; van de Löcht et al., 2020).

During the Paleoarchean, the amalgamated terranes were intruded by several generations of east-west oriented dolerite and norite dikes that are typically referred to as Ameralik dike swarm (Nutman et al., 2004). The mean age for the Ameralik dike swarms near the Isua area was given at 3421 ± 34 Ma (Rizo et al., 2012) although younger ages as low as 3265 ± 15 Ma have been reported elsewhere (Nutman et al., 2004).

Several ~3.08 to 2.84 Ga old greenstone belts and associated granitoid terranes were emplaced by horizontal tectonic processes during the Meso- and Neoarchean and are here represented by rocks from the ~3.08 Ga Ivisaartoq supracrustal belt as well as metavolcanic rocks from the ~2.97 Ga Ameralik Fjord region that were also cut by ~2.0 Ga dolerite dikes (Polat et al., 2009; Polat et al., 2010). Geochemical data and structural analysis (e.g., Kisters et al., 2012) for the Mesoarchean terranes revealed the influence of older recycled material, making a subduction zone-like setting the most likely geodynamic setting for the formation of these younger greenstone belts (Polat et al., 2011; Szilas et al., 2015a; Szilas et al., 2016; Szilas, 2018).
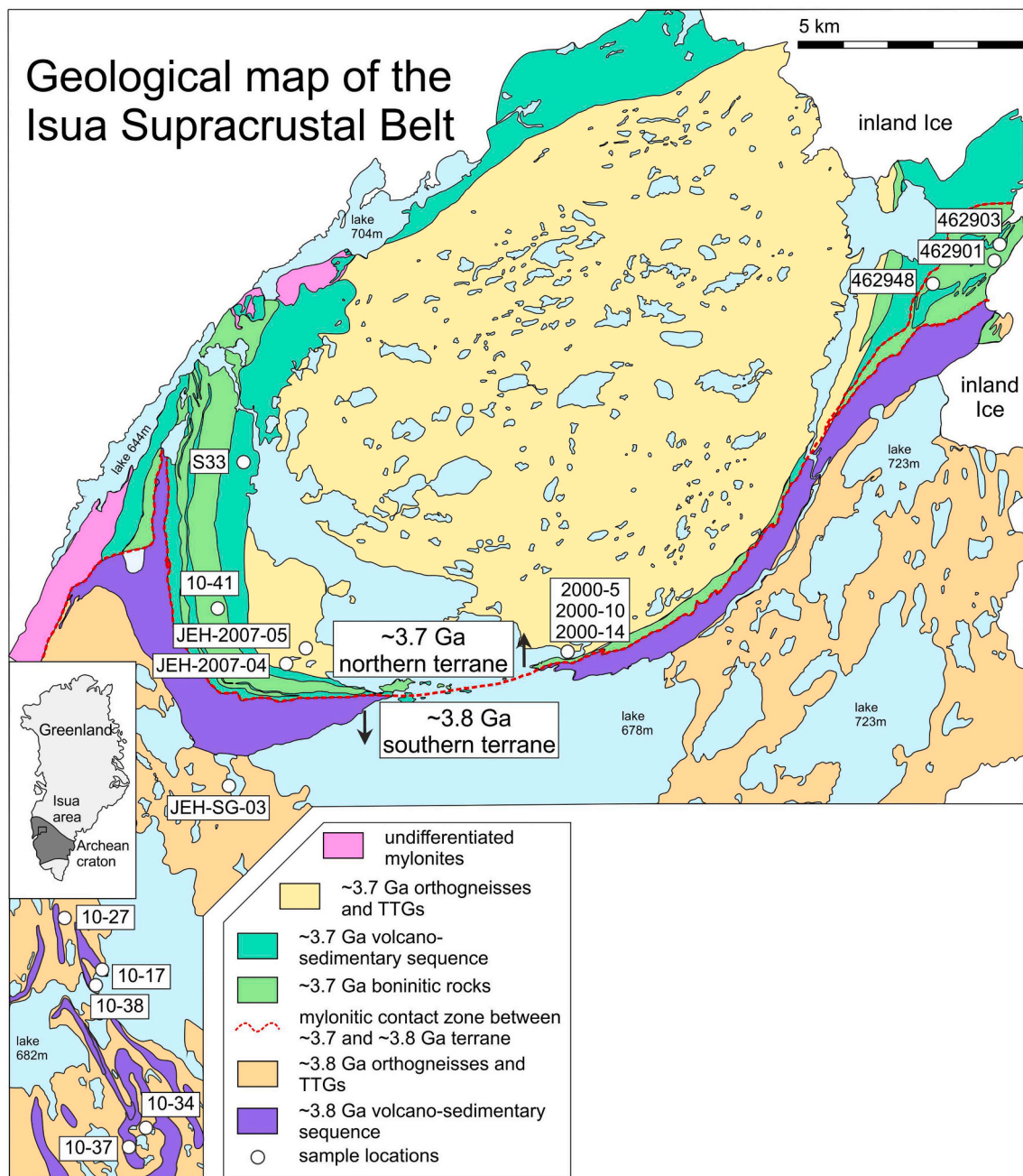
Fig. 1. Simplified geological map of the Isua region, including the Isua Supracrustal Belt (ISB) and sample locations from this study. Redrawn after Nutman and Friend, (2009) and Nutman et al., (2009). For locations of samples from the Ivisaartoq Supracrustal Belt and the Ameralik Fjord Region see Extended Data Fig. 1.

3. Methods

3.1. Sample dissolution and separation of clean Nd cuts

The dissolution of sample powders follows the chemical protocol of Tusch et al. (2019) and will only be summarized in brief (see Extended Data Table 1 and Extended Data Fig. 2). Each digestion involved 1 g of sample material that was dissolved in 15 ml 24 M HF + 15 ml 14 M HNO3 for 2 days at 140 °C and subsequently evaporated until near dryness. Subsequently, 5 ml 14 M HNO_3 were added and dried down to near dryness. This step was repeated three times to remove residual HF without forming insoluble fluoride precipitates. Afterwards, the samples were dissolved in 30 ml 6 M HCl at 120 to 150 °C for 48 h. In case of residual precipitates, this last step was repeated until clear sample solutions were obtained.

The separation for $^{142}Nd/^{144}Nd$ analysis follows a five-step ion exchange protocol to achieve maximum Nd purification (Extended Data Table 1). The first separation step (step I) follows the first-stage ion exchange column protocol of Tusch et al. (2019) and provides a rare earth element (REE) cut that is mostly free of matrix elements. In cases that required >1 g of sample material, REE cuts were combined after this separation step. In a next step (step II), REE were separated from the remaining matrix (mainly residual alkaline and alkaline earth metals) by using cation exchange resin and different HCl molarities. This matrix free REE cut was dried down and re-dissolved in 10 M HNO_3/20 mM $KBrO_3$ to fully oxidize Ce^{3+} to Ce^{4+}. Next (step III), Ce was separated from the remaining REE on Ln Spec resin, following a slightly modified separation protocol of Schnabel et al. (2017), where ≥99.95% of Ce is removed from the remaining light rare earth elements (LREE) cut. Subsequently, (step IV), separation step II was repeated, to remove the K

that was introduced by adding $KBrO_3$ during step III. Finally (step V), Nd was separated from the remaining LREE using 30 cm long glass columns that were filled with 6 ml of 50 μm Ln Spec resin. The columns were filled with 400 μl of anion resin on top in order to prevent the Ln Spec resin from floating up, which might broaden the eluted element peaks. This step purifies Nd from Pr and Sm as well as from residual Ce. In order to remove as much Pr as possible and losing the least Nd, we separately collected the last 3–5 ml before the expected onset of the Nd peak in 1 ml steps and analyzed 1‰ aliquots to determine Pr and Nd contents. Eventually, these 1 ml rinsing steps were added to the final Nd cut to obtain the highest Nd yields possible at low Pr monitors. This procedure allowed Nd yields of ~95% during separation step V, while ~75% of the Pr was removed. After separation steps II-V, we dried down the samples and treated the residues with 80 μl 14 M HNO_3 + 40 μl 30% H_2O_2 at low temperatures (≤ 60 °C) to destroy possible organic compounds.

To obtain comprehensive data sets, we also report long-lived ^{176}Lu—^{176}Hf and ^{147}Sm—^{143}Nd isotope data in addition to the long-lived isotope data reported in previous studies (Hoffmann et al., 2010; Hoffmann et al., 2011b; Hoffmann et al., 2011a; Hoffmann et al., 2014; Szilas et al., 2015a; Szilas et al., 2016; van de Löcht et al., 2018) for our sample collection. For long-lived ^{176}Lu—^{176}Hf and ^{147}Sm—^{143}Nd isotope measurements, 150 mg of sample powder were spiked with mixed ^{150}Nd—^{149}Sm and ^{176}Lu—^{180}Hf isotope tracers and digested in 8 ml 1:1 HF-HNO_3 for one day. After the first digestion step, samples were dried down, re-dissolved in 8 ml 1:1 HF-HNO_3 and digested in Parr© bombs at 180 °C for three days (Hoffmann et al., 2011a). Subsequently, samples were evaporated to near dryness before adding 5 ml of conc. HNO_3 that was immediately dried down to near dryness again. This step was repeated three times to effectively remove HF without forming insoluble fluoride precipitates. Next, samples were re-dissolved in 8 ml 6 M HCl in which they were fully dissolved. Pure fractions of Lu and Hf were obtained following the chemical separation protocol of Münker et al. (2001). A LREE-bearing cut was further separated from matrix elements by cation exchange using stage one from the separation protocol of Schnabel et al. (2017). From this LREE-bearing cut, pure fractions of Sm and Nd were obtained, following the chemical separation protocol of Pin and Zalduegui (1997) using Ln Spec resin.

3.2. Mass spectrometry

All Nd isotope measurements were performed on a Thermo Neptune Plus MC ICP-MS at Cologne. We used a 50 μl/min C-Flow Nebulizer (Savillex) that was connected to an ESI Apex Q desolvation system. For the Apex exhaust, we used an external peristaltic pump. The internal gas line of the Apex was connected to a N_2 gas line. The sample-out gas line of the Apex was attached to a Scott type double pass glass spray chamber by a 1.8 mm injector. In between the Apex and the injector, we connected an additional Ar gas line. We used H-skimmer cones as this has shown to ensure the most stable signals, typically yielding ~7 V on ^{142}Nd per 100 ppb Nd.

All seven Nd isotopes, ^{142}Nd, ^{143}Nd, ^{144}Nd, ^{145}Nd, ^{146}Nd, ^{148}Nd and ^{150}Nd were measured as well as ^{140}Ce and ^{147}Sm monitors to correct for isobaric interferences on masses ^{142}Nd, ^{144}Nd, ^{148}Nd and ^{150}Nd, respectively. For all Nd isotopes, faraday cups were connected to 10^{11} Ω amplifiers, while 10^{13} Ω amplifiers were used for faraday cups that monitored ^{140}Ce and ^{147}Sm. Mass bias was corrected by using the exponential law and either assuming a $^{146}Nd/^{144}Nd$ of 0.7219 or $^{148}Nd/^{144}Nd$ of 0.241578 (hereafter denoted as 6/4 or 8/4, respectively). If not explicitly noted otherwise, all reported $^{142}Nd/^{144}Nd$ isotope data were corrected for mass bias by using $^{148}Nd/^{144}Nd$. A gain calibration among the faraday cups and a baseline (1200 integration steps with 1.05 s each) was measured daily. Measurements were performed in static mode, since during use of dynamic mode 2 cup position are lost. As a consequence, all mass independent Nd masses could no longer be measured simultaneously. Measuring in dynamic mode could be applied in the near future with the new Neoma MC ICP-MS that has

11 cups. Individual measurements typically comprised 60 cycles (8.4 s integration time) and were usually run between 25 and 35 V on ^{142}Nd. Despite these high signals introduced into the cup, the retention rates for individual resistors did not fluctuate and measured Nd isotope compositions stayed constant during the measurements. Sample solutions were always bracketed by the referenced JNdi-1 standard solution and their intensity was matched typically within <5%. Individual samples were measured repeatedly (usually 10 to 12 times), eliminating possible fluctuations of gain and baseline values (see also Tusch et al. (2019)). Potential $^{141}Pr^1H$ interferences on mass 142 were checked by measuring a Pr-doped JNdi-1 at the beginning of each session and the general stability of the instrument was ensured by measuring an LP-1 in house standard (La Palma Basalt) at least every ~36 h (Extended Data Fig. 3). To be able to measure samples repeatedly at such high intensities, ~3 μg Nd were consumed per sample. The intensity of samples and JNdi-1 solutions were matched within ≤5% to each other and the analysis of samples and bracketing JNdi-1 solutions were interrupted by 200–300 s of wash time. Accordingly, the measurement time for one sample amounts to ~7 h. Procedural blanks for Nd were typically ranging between several 100 pg and a few ng, resulting in negligible blank contributions of ≤0.5% to the total analyte. The internal precision of one single measurement typically amounts to a 2 standard error of ±5, ±5, ±4, ±3 and ±8 ppm for $\mu^{142}Nd$, $\mu^{143}Nd$, $\mu^{145}Nd$, $\mu^{146}Nd$, and $\mu^{150}Nd$ values (8/4), respectively. Reported errors for repeatedly analyzed samples depict the 95% CI, although we consider our intermediate precision of ±1.4 ppm as minimum error for $^{142}Nd/^{144}Nd$ compositions (see section 5.2 for definition of intermediate precision).

For long-lived radiogenic isotope systematics, measured $^{143}Nd/^{144}Nd$ isotope data were mass bias corrected using the exponential law and assuming a $^{146}Nd/^{144}Nd$ ratio of 0.7219. All $^{143}Nd/^{144}Nd$ data are reported relative to the La Jolla reference material, having a $^{143}Nd/^{144}Nd$ composition of 0.511859 which is equivalent to a $^{143}Nd/^{144}Nd$ composition of 0.512115 for the JNd-1 reference material. Our intermediate precision for $^{143}Nd/^{144}Nd$ compositions amounts to ±0.4 ε-units and is considered as minimum uncertainty for $^{143}Nd/^{144}Nd$ analysis. Hafnium isotope analyzes were corrected using the exponential law and assuming a $^{179}Hf/^{177}Hf$ of 0.7325. All data are given relative to the Münster AMES JMC, having a $^{176}Hf/^{177}Hf$ ratio of 0.282160. The intermediate precision on $^{176}Hf/^{177}Hf$ isotope ratios amounts to ±0.4 ε-units. The errors on the parent/daughter ratios amount to 0.2%. Our quoted errors for initial Nd and Hf isotope compositions involve the errors from our intermediate precision, errors on parent/daughter ratios, and errors on the crystallization ages. All data are reported relative to the average chondritic values of Bouvier et al. (2008). Total procedural blanks were 35 pg for Nd, 56 pg for Sm, 41 pg for Lu and 26 pg for Hf.

4. Results

We have obtained $^{142}Nd/^{144}Nd$ isotope data for a variety of previously investigated Archean samples from southwest Greenland, as well as for some modern rocks (including certified reference materials) and standard solutions. The dataset includes 17 different felsic to mafic-ultramafic rocks and 4 replicates that lie within the IGC (SOISB, ISB and Ameralik dike swarm). Measured $\mu^{142}Nd$ values for individual ~3.72 to ~3.8 Ga samples range from +9.2 ± 2.6 to +13.6 ± 1.4, giving a mean value of +11.2 ± 3.4 which is in excellent agreement with results from previous studies (Fig. 2a) (Boyet and Carlson, 2006; Caro et al., 2006; Bennett et al., 2007; Rizo et al., 2011; Saji et al., 2018). This value also overlaps with the $\mu^{142}Nd$ composition of one sample from the Narssaq ultramafic body of similar age ($\mu^{142}Nd = +11.6 \pm 2.2$). Mantle-derived samples from ~3.8 Ga enclaves in the SOISB area yield slightly, but resolvable higher $\mu^{142}Nd$ values of +13.0 ± 1.1 when compared to mantle-derived rocks from the ~100 Ma younger northern ~3.7 ISB terrane ($\mu^{142}Nd = +9.8 \pm 1.0$). This younger terrane includes tholeiites and boninites, both showing indistinguishable $\mu^{142}Nd$ values that are in

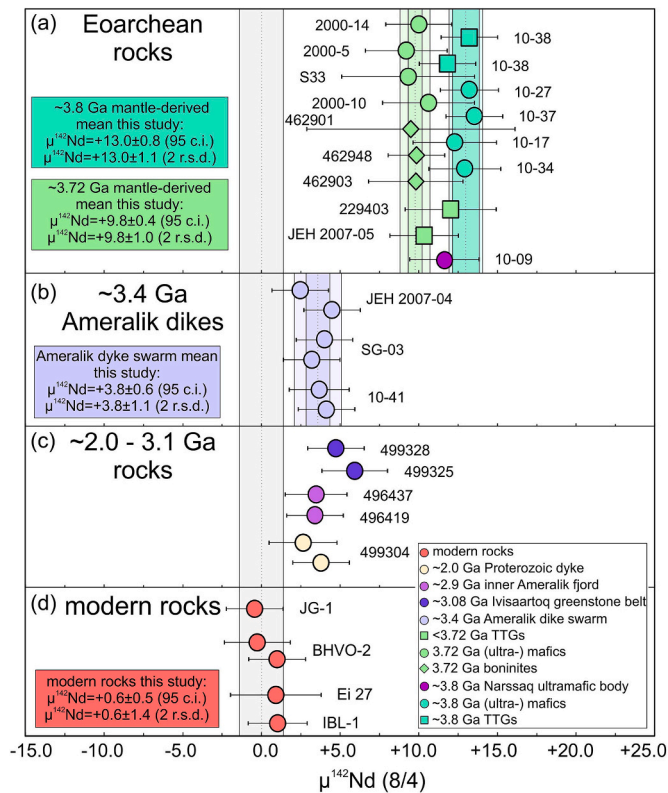**Fig. 2.** $^{142}Nd/^{144}Nd$ isotope compositions of samples from SW Greenland and modern rocks. a) Comparison of ~3.7 and ~ 3.8 Ga rocks from the ISB All mean values obtained here overlap within error with previous studies (e.g., Boyet and Carlson, 2006; Caro et al., 2006; Bennett et al., 2007; Rizo et al., 2011; Rizo et al., 2012; Rizo et al., 2013; Saji et al., 2018). However, ~3.8 Ga mafic-ultramafic rocks from this study exhibit $\mu^{142}Nd$ excesses that can be statistically resolved from ~3.72 Ga mantle-derived rocks. One sample from the Narssaq Ultramafic body (NUB) also reveals similar $\mu^{142}Nd$ excesses as ~3.7 to ~3.8 Ga Isua rocks, in line with their proposed Eoarchean age (van de Löcht et al., 2020). b) Compositions of ~3.4 Ga Ameralik dike swarm samples c) $^{142}Nd/^{144}Nd$ isotope composition of Mesoarchean to Proterozoic rocks from SW Greenland. d) $^{142}Nd/^{144}Nd$ isotope composition of various modern terrestrial rocks and reference materials. The grey error band drawn throughout the figure depicts the intermediate precision of ±1.4 ppm (2 r.s.d.). Errors shown for individual samples are the 95% CI intervals, our intermediate precision of ±1.4 ppm is considered as minimum error.

good agreement with previously reported $\mu^{142}Nd$ values for these boninites (O'Neil et al., 2016). In addition, we have measured three samples from the Ameralik dike swarm (including replicate digestions) that yield homogeneous $\mu^{142}Nd$ compositions of +3.8 ± 1.1. This mean value is also indistinguishable from the value obtained by Saji et al. (2018) ($\mu^{142}Nd$ = +4.9 ± 1.8; Fig. 2b). Our studied samples also comprise younger Mesoarchean and Proterozoic rocks from SW Greenland. Two mafic rocks from the ~3.08 Ga Ivisaartoq supracrustal belt, two mafic rocks samples from the 2.97 Ga Ameralik fjord region as well as one ~2.0 Ga old dike (including one replicate) from SW Greenland all bear small excesses in $\mu^{142}Nd$, ranging from +5.9 ± 2.1 to +2.7 ± 2.2 (Fig. 2c). To obtain a coherent set of coupled $^{143,142}Nd$ and ^{176}Hf data, samples that lack available ^{147}Sm—^{143}Nd or ^{176}Lu—^{176}Hf isotope data were also analyzed here (including all Ameralik dikes and the ~2.0 Ga Proterozoic dike). Ameralik dikes generally have strongly homogeneous $\varepsilon^{143}Nd_{(i)}$ values of +1.9 ± 0.4 to +2.4 ± 0.4, in good agreement with previous studies (Saji et al., 2018). Calculated $\varepsilon Hf_{(i)}$ values range from +2.6 ± 0.4 to +2.9 ± 0.4. In contrast, the 2.0 Ga dike shows lower $\varepsilon^{143}Nd_{(i)}$ (+0.2 ± 0.4) and $\varepsilon Hf_{(i)}$ values (+0.8 ± 0.4), respectively.

Furthermore, two individual digestions of the geological reference material BHVO-2 yield $\mu^{142}Nd$ values of −0.2 ± 2.1 and + 1.0 ± 1.8, respectively, in excellent agreement with previous results (Saji et al., 2016; Schneider et al., 2018; Hyung and Tissot, 2021). To further validate our method, we also measured the $\mu^{142}Nd$-$\mu^{143}Nd$ compositions for our different digestions of reference material BHVO-2 that was doped with variable amounts of sample 10–38, having an average $\mu^{142}Nd$ value of +12.5 ± 2.0. Prior to digestion, sample powders were mixed at different proportions (25%, 50% and 75% of added BHVO-2). These mixing ratios should have resulted in $\mu^{142}Nd$ excesses of ~ + 9, +6 and + 3 ppm, respectively, and are in good agreement with our measured values of +8.0 ± 1.7, +5.5 ± 1.8 and + 1.6 ± 1.9, respectively. The analysis of the La Jolla reference material yields slightly elevated $\mu^{142}Nd$ values of +2.6 ± 2.5, in perfect agreement with previous results (Saji et al., 2016). Praseodymium-doped JNdi-1 standards measured here never revealed resolvable anomalous $\mu^{142}Nd$ compositions (−0.9 ± 3.6 to +1.3 ± 1.4). We have also measured several modern rock samples and certified reference materials (Fig. 2d), including one intraplate basalt from the Eifel volcanic field in Germany (Ei-27), one intraplate basalt from the Hyblean Plateau in Italy (IBL-1), as well as the granite reference material JG-1 that all have modern day $\mu^{142}Nd$ values of +0.9 ± 2.9, +1.0 ± 1.9 and − 0.4 ± 1.4, respectively.

5. Discussion

5.1. Interferences and mass-independent isotope effects

High precision Nd isotope measurements are hampered by four isobaric interferences (^{142}Ce, ^{144}Sm, ^{148}Sm and ^{150}Sm). Due to the highly efficient redox chemistry (step III) and the final REE separation (step V), Ce monitors in our samples were always smaller than Ce monitors in our standard solutions ($^{142}Ce/^{142}Nd$ typically below 4 × 10^{-7}), except for three samples that had insignificantly higher Ce interferences. For Sm interferences on mass 144, 148 and 150, our samples had always lower Sm monitors than our standard solutions, typically having a $^{144}Sm/^{144}Nd$ of 2 × 10^{-6}. Measurements of Ce and Sm doped standards (0.02 ng/ml Sm or Ce at 400 ng/ml Nd exceeding maximum $^{142}Ce/^{142}Nd$ and $^{144}Sm/^{144}Nd$ monitors of any measured samples analyzed here) yielded $^{144}Sm/^{144}Nd$ and $^{142}Ce/^{142}Nd$ ratios of 2 × 10^{-5}. Both doped standards yielded $\mu^{142}Nd$ (8/4) values that were indistinguishable from zero (−0.4 ± 3.4 for Sm-doped JNdi-1, and + 0.6 ± 2.4
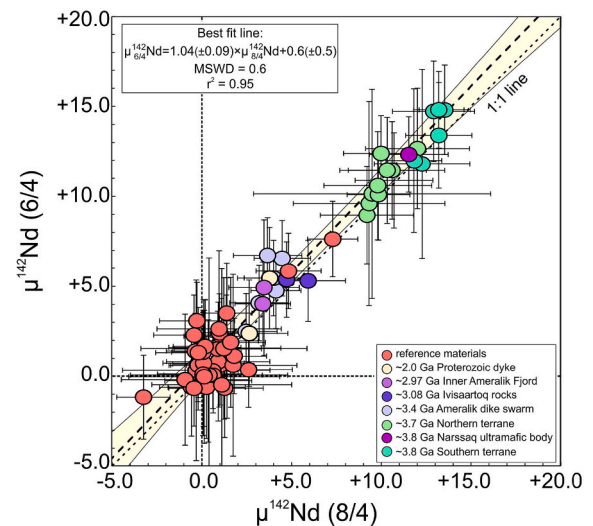

Fig. 3. Comparison of $^{148}Nd/^{144}Nd$ vs. $^{146}Nd/^{144}Nd$ corrected $^{142}Nd/^{144}Nd$ data that are expected to plot on a 1:1 line. The best-fit line intersects the x-axis at +0.6 ± 0.5 with a slope of +1.04 ± 0.09, implying that both mass bias corrections work properly.

for Ce-doped JNdi-1). In addition, 8/4 and 6/4 corrected ^{142}Nd/^{144}Nd data always overlap within error with each other, further arguing against any analytical artifacts introduced by potentially insufficient Sm interference corrections (Fig. 3).

In addition to isobaric interferences, ^{142}Nd/^{144}Nd analysis can be compromised by molecular interference of ^{141}PrH$^+$ on ^{142}Nd as previously shown by Saji et al. (2016). To be able to eliminate analytical artifacts of ^{141}PrH$^+$ on ^{142}Nd, we measured a Pr-doped JNdi-1 standard solution at the beginning of each measurement session that had Pr/Nd ratios slightly higher than chondritic (Pr:Nd > 1:7) which would be expected for highly enriched samples that underwent insufficient Pr—Nd separation during chemical purification procedures. Surprisingly, measured Pr-doped standard solutions never revealed detectable analytical artifacts on ^{142}Nd, although Saji et al. (2016) reported excesses of up to ~ + 9 ppm in Pr-doped standard solutions with chondritic Pr/Nd ratios. Although the reason for this discrepancy remains unknown, we speculate that this could be linked to the combination of a Jet sample cones with an X-skimmer cone (as used by Saji et al. (2016)) which might facilitate the formation of ^{141}Pr$^+$ interferences.

For high precision isotope measurements, high yields during chemical separation are essential. First, high yields allow performing replicate measurements at the highest signal intensities possible. Secondly, loss of material during ion exchange chromatography can induce mass-independent isotope effects that might not be fully correctable and may therefore cause artificial isotope anomalies (Thirlwall, 1991; Wombacher and Rehkämper, 2003). This is in accord with our findings for the first 15% yield fraction of an LP-1, partly eluted during separation step V (LN spec resin). This cut bears strong mass-independent excesses of higher masses (μ^{150}Nd (6/4) = +45.3 ± 5.4) and deficits (although not clearly resolvable) on μ^{142}Nd (6/4) (−4.1 ± 4.8 ppm). This finding is in excellent agreement with findings by Saji et al. (2016) who have conducted equivalent tests using the same ion exchange resin. These authors have concluded that this fractionation pattern is produced by nuclear field shift, in accord with results by Garçon et al. (2018), who observed similar nuclear field shift-induced fractionation patterns for Nd isotopes.

The mass-independent fractionation caused by nuclear field shift might also be responsible for small deficits in μ^{150}Nd values found in some of our samples. Generally, the fractionation of ^{150}Nd/^{144}Nd ratios can be avoided by using DGA resin (Wang and Carlson, 2022), although over the course of this study, the fractionation of ^{150}Nd/^{144}Nd ratios was also prevented by having yields >99.5% using the LN spec resin (separation step V). For samples with fractionated ^{150}Nd/^{144}Nd ratios, it has to be evaluated if μ^{142}Nd values would also be affected by nuclear field shift-induced fractionation, since our mass bias correction relies on accurate and unfractionated ^{148}Nd/^{144}Nd ratios. In contrast to slightly more variable μ^{150}Nd (8/4) values obtained for replicate LP-1 analysis (+3.0 ± 4.7 to −13.2 ± 1.6), measured μ^{148}Nd values (6/4) remain unfractionated and exhibit less variation (−3.3 ± 2.8 to +3.9 ± 2.7). The LP-1 analysis with the strongest measured μ^{150}Nd (8/4) deficit of −13.4 ± 3.4 ppm still retains μ^{142}Nd (8/4) and μ^{142}Nd (6/4) values of +0.1 ± 2.3 and + 0.7 ± 3.5, respectively, indistinguishable from our long-term average for this reference material (μ^{142}Nd (8/4) = +0.4 ± 1.4 and μ^{142}Nd (6/4) = +1.1 ± 2.1; 2rsd, N = 23) (Extended Data Fig. 3). This implies that even fractionated μ^{150}Nd values as low as −13 ppm did not induce any resolvable effects on ^{142}Nd/^{144}Nd compositions. Only one sample (JEH 2007–04) revealed an even higher magnitude of ^{150}Nd/^{144}Nd fractionation, yielding a μ^{150}Nd (8/4) value of −14.6 ± 2.3. However, a replicate digestion and analysis of this sample revealed identical μ^{142}Nd (8/4) (+4.5 ± 1.6 and 4.0 ± 1.6) and μ^{142}Nd (6/4) values (+6.6 ± 1.7 and + 5.5 ± 1.5) at less fractionated μ^{150}Nd (8/4) Nd values (−10.3 ± 3.7). Since fractionated ^{150}Nd/^{144}Nd compositions of less than −15 ppm did not induce any artificial effects on μ^{142}Nd (8/4) values, we take this as evidence that these effects on ^{142}Nd/^{144}Nd analysis are negligible, considering the magnitude of mass-independent Nd isotope fractionation induced by our analytical protocol. An

insignificant contribution by nuclear field shift effects on ^{148}Nd isotope abundances is further verified by inspecting both, ^{146}Nd/^{144}Nd and ^{148}Nd/^{144}Nd corrected ^{142}Nd/^{144}Nd data, as the two mass bias corrections involved yield identical ^{142}Nd results. This is illustrated in Fig. 3, where all samples plot on the predicted 1:1 line in μ^{142}Nd (6/4) vs. ^{142}Nd (8/4) space. We therefore conclude that a slight contribution of nuclear field shift might explain the observed scatter in ^{150}Nd isotope abundances for our LP-1 in-house reference sample (and some other samples). As demonstrated above, however, such effects are negligible for ^{148}Nd/^{144}Nd and consequently do not affect mass bias corrected ^{142}Nd/^{144}Nd ratios, for which the variations are only caused by statistical errors.

5.2. Method verification

Resolving isotope compositions at the lower ppm level is challenging due to the different interference and mass-independent isotope effects described above. In order to carefully validate our separation and measurement protocol we took three approaches. (1) In order to cross-reference with previous studies (Boyet and Carlson, 2006; Caro et al., 2006; Bennett et al., 2007; Rizo et al., 2016; Saji et al., 2018), we measured ~3.72 to 3.8 Ga old Isua rocks and ~ 3.4 Ga Ameralik dikes that were most recently shown to exhibit homogenous μ^{142}Nd excesses of +10.5 ± 1.8 ppm and + 4.7 ± 1.7, respectively (Saji et al., 2018) (Fig. 2a and b). (2) Additionally, we doped an ^{142}Nd excess-bearing sample (10–38) with an excess-free terrestrial certified reference material (BHVO-2) to verify that we can resolve small predicted anomalies (Fig. 4). (3) We performed repeated analysis of multiple digestions of our in-house reference material LP-1 to obtain an intermediate precision for ^{142}Nd/^{144}Nd analysis (Extended Data Fig. 3).

Individual ~3.7–3.8 Ga old Isua samples from this study exhibit μ^{142}Nd values that range from +9.2 ± 2.6 to +13.6 ± 1.4. Our ~3.7–3.8 Isua rocks yield a mean μ^{142}Nd value of +11.2 ± 3.4, whichs in good agreement with the mean MC ICP-MS value obtained by Saji et al. (2018) (μ^{142}Nd = 10.7 ± 1.8) and with the results from previous TIMS studies (Boyet and Carlson, 2006; Caro et al., 2006; Bennett et al., 2007; Rizo et al., 2016) (Fig. 2a). Furthermore, replicate digestions and isotope measurements conducted for three different Ameralik dike samples in
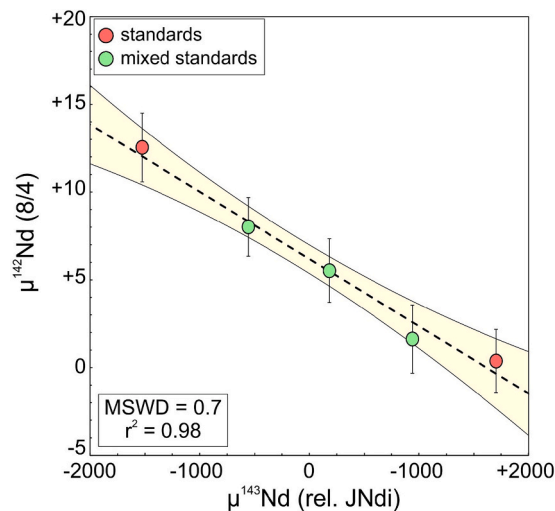

Fig. 4. Measured μ^{142}Nd vs. μ^{143}Nd compositions for processed reference material BHVO-2 that was doped with different amounts of SW Greenland sample 10–38 (green). Mean values for sample 10–38 (μ^{142}Nd = 12.5 ± 2.0)) and BHVO-2 (+0.4 ± 1.8) are taken from this study (red). Errors for mixed standards are the same as in Fig. 3 and for the two standard endmember compositions, the 2 r.s.d. from their respective mean value was used. (For interpretation of the references to colour in this figure legend, the reader is referred to the web version of this article.)

duplicates (10–41, SG-03 and JEH 2007–04) overlap with each other within ≤0.5 ppm. The mean μ^{142}Nd value for our Ameralik dike samples amounts to $+3.8 \pm 1.1$ and is in excellent agreement with the mean value obtained by (Saji et al., 2018) (μ^{142}Nd = $+4.7 \pm 1.7$), but does not confirm the strongly heterogeneous compositions reported by Rizo et al. (2012) (Fig. 2b). Considering the strongly fractionated mass-independent Nd isotope compositions (μ^{150}Nd up to $+42.4$; μ^{145}Nd up to $+15.3$) reported by Rizo et al. (2012), we speculate that their negative ^{142}Nd/^{144}Nd isotope compositions reported for Ameralik dikes may rather be related to unaccounted analytical effects, a conclusion that was previously also drawn by (Saji et al., 2018).

The results of the mixing test of the excess-bearing sample 10–38 mixed with different amounts of BHVO-2 reference material are also in good agreement with the expected ^{142}Nd/^{144}Nd compositions. When plotted in μ^{142}Nd vs. μ^{143}Nd space, combined powders of BHVO-2 and sample 10–38 define a straight mixing line between the respective endmember compositions, demonstrating the accuracy and precision of our data (Fig. 4).

Finally, we have measured juvenile volcanic rocks that are not expected to carry anomalous ^{142}Nd/^{144}Nd compositions, comprising one intraplate basalt from the Quaternary Eifel volcanic field in Germany (Ei-27), one intraplate basalt from the Hyblean Plateau on Sicily (IBL-1) as well as the two terrestrial reference materials JG-1 and BHVO-2 (Fig. 2d). Our results for BHVO-2, including a replicate analysis, amount to a mean μ^{142}Nd = $+0.4 \pm 1.8$ (2r.s.d.), in excellent agreement with previous data (Burkhardt et al., 2016; Saji et al., 2016; Garçon et al., 2018; Schneider et al., 2018; Hyung and Tissot, 2021; Wang and Carlson, 2022). Furthermore, the analysis of a La Jolla reference material reveal mass-independent isotope effects for the different Nd masses (μ^{142}Nd = $+2.6 \pm 2.5$, μ^{145}Nd = -5.7 ± 2.1 and μ^{150}Nd = $+13.3 \pm 4.3$), also in good agreement with previous MC ICP-MS results (Saji et al., 2016) that are possibly linked to fractionation introduced during the purification process (Wakaki and Tanaka, 2012). Multiple analysis ($N = 23$) of seven different digestions from our in-house reference material LP-1 (historical La Palma basalt) that were processed and analyzed together with our samples, were used to determine our intermediate precision. They yield an average μ^{142}Nd value of $+0.5 \pm 1.4$ (2r.s.d.) and $+1.0 \pm 2.2$ (2r.s.d.) if normalized to 8/4 and 6/4, respectively (Extended Data Fig. 3). We consider this intermediate precision as minimum error for our ^{142}Nd/^{144}Nd measurements. Due to its superior intermediate precision, we prefer the 8/4 correction, and, if not stated otherwise this normalization is used hereafter.

5.3. Age significance of μ^{142}Nd excesses in Greenland rocks

5.3.1. ^{142,143}Nd differentiation model ages
Coupled ^{147,146}Sm–^{143,142}Nd isotope systematics are a powerful tool to unravel planetary silicate differentiation processes. By combining these two decay series, it is possible to determine the timing of ancient mantle depletion, since the slope in μ^{142}Nd and ε^{143}Nd$_{(i)}$ space is a function that depends on the differentiation age (e.g., Harper and Jacobsen, 1992; Caro et al., 2003; Boyet and Carlson, 2005; Bennett et al., 2007). However, this application relies on determining accurate μ^{142}Nd and ε^{143}Nd$_{(i)}$ values of a mantle reservoir at a given age and typically assumes single stage silicate differentiation.

The major problem for calculating accurate ^{142,143}Nd/^{144}Nd model ages arises from inaccurate initial ε^{143}Nd$_{(i)}$ values (Fig. 5). To minimalize these effects, we did not extrapolate samples to one uniform crystallization age, since the calculation of ε^{143}Nd$_{(t)}$ values at any other time than their crystallization ages creates biased ε^{143}Nd$_{(t)}$ values. Instead, we have only considered samples that cluster in a very narrow age range ($\leq \pm 30$ Ma), causing insignificant propagated uncertainties on ε^{143}Nd$_{(i)}$ values. Moreover, TTGs were excluded here, since they are the product of remelting older precursor rocks (Hoffmann et al., 2011a). Schneider et al. (2018) were able to show that the variations in μ^{142}Nd found in TTGs often seem to have a higher magnitude compared to
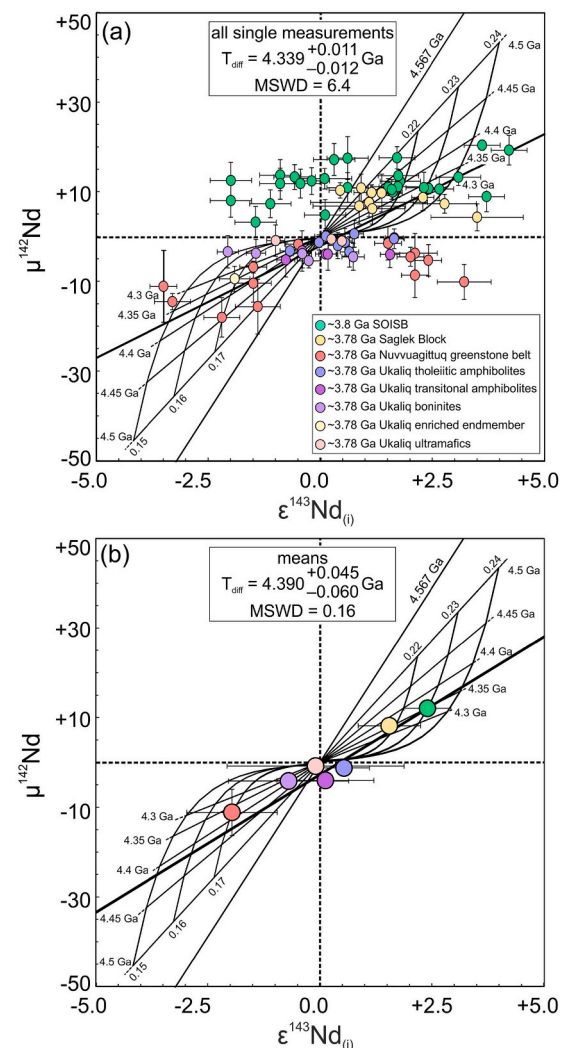

Fig. 5. Plot illustrating coupled ^{142}Nd—^{143}Nd data and calculated differentiation model ages for samples from the North Atlantic Craton and the Superior Province. a) Plot showing all data from the SOISB, Saglek Block, Superior Province and the Ukaliq Supracrustal Belt, (Bennett et al., 2007; O'Neil et al., 2008; Rizo et al., 2013; Caro et al., 2017; Morino et al., 2018; Saji et al., 2018). b) Same as in a) but using means and 95% CI on the means as errors. Data with resolvable negative μ^{142}Nd values at ε^{143}Nd$_{(i)} \geq +2$ are excluded here since these data clearly indicate open system behavior of the ^{147}Sm—^{143}Nd system or multi-stage evolution. Further, ε^{143}Nd for one sample from this study (10–34), one sample from the Saglek Block (LA11–08; Morino et al. (2017)), one sample from (JG03/52; Bennett et al., 2007)) and all samples measured by Rizo et al. (2013) were excluded since they plot in the forbidden range of the isochron that require differentiation ages >4.567 Ga. Since this should not have affected μ^{142}Nd values, these samples were still used to calculate μ^{142}Nd mean values. We only included mantle-derived rocks that fall in an age range of 3.78 ± 0.03 Ga. For the Isua greenstone belt, this only included a subset of samples from Bennett et al. (2007) and Saji et al., (2018). For a better overview of the data that was considered here to calculate means, they are listed in supplementary file S4. Errors displayed for individual samples are the same as in Fig. 3 and those that are given in each study.

contemporaneous mantle-derived rocks, which would cause further bias in our dataset (Fig. 2a). This is also indicated by a 3.715 Ga metadiorite sample from this study (229403) that seems to have slightly higher μ^{142}Nd values compared to contemporaneous mafic-ultramafic rocks (Fig. 2a). Furthermore, a variable crustal residence time between emplacement of the mafic precursor rocks and subsequent TTG extraction can also lead to variable ε^{143}Nd$_{(i)}$ values, causing further scatter in this model age approach.

For the reasons discussed above, we only consider mantle-derived samples that fall into a narrow age range of 3.800 ± 0.030 Ga. As already suggested in previous studies, we have also included ^{142}Nd—^{143}Nd data from the Eastern Superior Craton as they were likely affected by the same differentiation event (Caro et al., 2017; Morino et al., 2017; Saji et al., 2018). This way we consider a statistically significant population and can combine our data with literature data from the near-contemporaneous ~3.78 Ga Saglek Block and the 3.78 Ga Nuvvuagittuq Greenstone Belt (O'Neil et al., 2008; Morino et al., 2017) to infer a differentiation model age for the North Atlantic Craton and Eastern Superior Province. Despite the ongoing debate as to whether the Nuvvuagittuq greenstone belt might have preserved an ^{146}Sm—^{142}Nd isochron age of 4.28 Ga (O'Neil et al., 2008), long-lived isotope systematics have rather argued for an Eoarchean ~3.8 Ga age for the Nuvvuagittuq greenstone belt (Guitreau et al., 2013; Roth et al., 2013), in accordance with zircon age populations from the same supracrustal successions that are always younger than 3.78 Ga (Cates et al., 2013). We have also included samples from the Ukaliq supracrustal belt (Caro et al., 2017) that has a close genetic link to and a similar emplacement age as the ~3.78 Ga Nuvvuagittuq Greenstone Belt (Cates et al., 2013; Chowdhury et al., 2020). Our inferred model age including all samples amounts to $4.339^{+0.011}_{-0.012}$ Ga which is in good agreement with the previously reported model ages ranging from ~4.32 to ~4.53 Ga (Caro et al., 2003; Boyet and Carlson, 2005; Caro et al., 2006; Bennett et al., 2007; Rizo et al., 2011; Morino et al., 2017; Morino et al., 2018; Saji et al., 2018), although errors seem to be unrealistically low and a high MSWD of 6.4 reveals strong scatter of the best fit line (Fig. 5a). Notably the highest inferred model ages of ~4.5 Ga (Boyet and Carlson, 2005; Bennett et al., 2007; Rizo et al., 2012) are linked to the assumption that bulk Earth has a 20 ppm lower μ^{142}Nd composition (similar to that of ordinary chondrites), where differentiation ages were calculated by drawing an array between that composition and the depleted Isua composition. This created steeper slopes in the ^{142}Nd—^{143}Nd arrays leading to higher inferred differentiation model ages.

Despite our screening, accurate ^{142}Nd—^{143}Nd differentiation model ages are still hampered by the large scatter of ε^{143}Nd$_{(i)}$ values (Fig. 5). This could imply that in some samples the long-lived ^{147}Sm—^{143}Nd systematics have been modified by multiple differentiation events, magma mixing (i.e., added slab melts or crustal contamination) or post-magmatic alteration (e.g., Moorbath et al., 1997; Frei et al., 2002; Hoffmann et al., 2011b; Caro et al., 2017). For example, one sample from this study (10–34), and one sample from the Saglek block (Morino et al., 2017) even plot in the forbidden zone of the model age regression (Fig. 5a). This would also be the case for sample PB-3 from (Saji et al., 2018) although it has not been included here as it belongs to the younger ~3.7 Ga ISB sequence. On the other hand, some of the samples from the Nuvvuagittuq Greenstone Belt (O'Neil et al., 2008) have positive ε^{143}Nd$_{(i)}$ of ~ + 2 despite having negative μ^{142}Nd values. When only considering mean values for different localities as suggested earlier (Caro et al., 2017; Morino et al., 2017; Saji et al., 2018), the inferred global differentiation model age amounts to $4.390^{+0.045}_{-0.060}$ Ga (Fig. 5b). Using means for different sample localities seems to provide the best way to calculate coupled ^{142,143}Nd differentiation ages as the errors of the averaged ε^{143}Nd$_{(i)}$ values for different localities will increase with increasing ε^{143}Nd$_{(i)}$ heterogeneity. Consequently, a higher scatter in ε^{143}Nd$_{(i)}$ values will cause a higher error for the inferred mean values that will be weighted less when calculating error propagated differentiation model ages, leading to more realistic estimates of accompanying errors. We conclude that the calculation of accurate and precise ^{142}Nd—^{143}Nd differentiation model ages is not limited by the precision of ^{142}Nd/^{144}Nd analysis but is mainly controlled by ε^{143}Nd$_{(i)}$ values that might have been modified by multiple younger differentiation events or post-magmatic alteration. For this reason, the $4.426^{+0.084}_{-0.064}$ Ga differentiation age seems the most plausible since it offers the best possibility to account for modified ε^{143}Nd$_{(i)}$ values. This age is also in good agreement with terrestrial differentiation age estimates that were inferred from independent isotope approaches (Wilde et al., 2001; Allègre et al., 2008; Mukhopadhyay, 2012).

5.3.2. Origin of combined εHf$_{(i)}$- ε^{143}Nd$_{(i)}$- μ^{142}Nd patterns

Eoarchean rocks from the Isua area are known to exhibit decoupled εHf$_{(i)}$- ε^{143}Nd$_{(i)}$ values, showing predominantly elevated εNd$_{(i)}$ values at near-chondritic εHf$_{(i)}$ values (Bennett et al., 1993; Hiess et al., 2009; Hoffmann et al., 2011b; Rizo et al., 2011; Rizo et al., 2019). For a long time, it has been argued whether or not this decoupling (especially in the Isua region) is a pristine magmatic (source) feature or if it was induced during late-stage metamorphism (Bennett et al., 1993; Moorbath et al., 1997; Bennett et al., 2007; Hoffmann et al., 2010; Hoffmann et al., 2011b; Rizo et al., 2011; Hoffmann et al., 2012; Hoffmann et al., 2014; Rizo et al., 2016; van de Löcht et al., 2020). Our high precision ^{142}Nd/^{144}Nd isotope data can shed new light on this debate. Previous studies invoked three scenarios to explain the observed Hf—Nd isotope decoupling: (I) Perovskite fractionation in a deep magma ocean (Rizo et al., 2011); (II) late-stage metamorphism (Hoffmann et al., 2011b), (III) source processes in a subduction zone-like setting (Hoffmann et al., 2011b; van de Löcht et al., 2020) or (IV) garnet-controlled Hf—Nd decoupling (Hoffmann et al., 2010; Kamber and Tomlinson, 2019). Scenario IV can be ruled out for the Isua rocks, because garnet fractionation rather produces highly radiogenic ^{176}Hf/^{177}Hf isotope compositions (e.g., Hoffmann et al., 2010; Hoffmann and Wilson, 2017; Kamber and Tomlinson, 2019; Hasenstab et al., 2021). In the following, we will evaluate the effects on long- and short-lived isotope systematics for the other three models based on data from this study and previous long-lived Hf and Nd isotope data (Hoffmann et al., 2010; Hoffmann et al., 2011b; van de Löcht et al., 2020).

5.4. Role of perovskite fractionation

It has been experimentally shown (e.g., Corgne et al. (2005)) that extensive crystallization of Ca and Mg perovskite can severely fractionate high field strength elements (HFSE) from REE. While both minerals have $D_{Sm}/D_{Nd} > 1$, Ca perovskite has a $D_{Lu}/D_{Hf} > 1$ whereas Mg perovskite has a $D_{Lu}/D_{Hf} < 1$. Depending on the proportions of Ca and Mg perovskite crystallized, previous studies have postulated that decoupled Hf and Nd isotopes in the Isua area might be linked to a perovskite-related origin (Caro et al., 2005; Hoffmann et al., 2011b; Rizo et al., 2011). To re-evaluate these previous models, we have re-modelled trace element compositions as well as ^{176}Hf-^{142,143}Nd isotope systematics during Ca—Mg perovskite crystallization. In our modelling approach we use coherent partition coefficients presented by Corgne et al. (2005) and a range of Ca—Mg perovskite proportions that were recently proposed for the terrestrial magma ocean (2% to 10% Ca-perovskite) (Caro et al., 2005; Hoffmann et al., 2011b; Rizo et al., 2011). We assumed different degrees of equilibrium crystallization (5 to 50%) and a primitive mantle as starting composition (Palme and O'Neill, 2013) (see supplementary file S2 for partition coefficients, trace elements and isotope results). Our modelling approach demonstrates that models, which invoke perovskite fractionation as origin for decoupled Hf and Nd isotopes, reveal three major problems:

(1) Both, Ca- and Mg-perovskite would severely fractionate Th—Ti and HFSE from REE, creating diagnostic geochemical fingerprints such as strongly fractionated Th/La ratios, Zr—Hf and Nb—Ta anomalies (also see Extended Data Figs. 4 and 5). In this regard, invoking perovskite cumulates as source for Isua rocks (Caro et al., 2005; Hoffmann et al., 2011b; Rizo et al., 2011) conflicts with observational constraints. Ubiquitous negative Nb—Ta anomalies in Isua rocks are inconsistent with a perovskite cumulate origin that would produce no or slightly positive Nb—Ta anomalies. Moreover, other HFSE-related geochemical signatures (e.g. Zr—Hf anomalies) argue strongly against a perovskite involvement in the petrogenesis of Isua rocks, as positive Zr—Hf anomalies should be directly coupled with negative εHf$_{(i)}$ values (and vice versa), a feature that is not observed in Isua rocks (Extended Data

Fig. 4a). The segregation of perovskite cumulates as suggested by previous studies (Caro et al., 2005; Hoffmann et al., 2011b; Rizo et al., 2011) would be characterized by very uniform Nb/Ta ratios of ~10, and Zr/Hf ratios of 33 to 34, fairly independent of Ca and Mg pervoskite proportions or crystallization grades. However, previous studies that have obtained high precision isotope dilution data for Nb/Ta ratios have hardly reported any samples with Nb/Ta ratios as low as 10 (Hoffmann et al., 2010; Tusch et al., 2019; van de Löcht et al., 2020). The vast majority of Isua rocks display higher and variable Nb/Ta ratios that often reach values >14. Moreover, many ISB rocks have significantly lower Zr/Hf ratios than 33, with ratios as low as 28, in good agreement with those of modern day MORBs (Münker et al., 2003). The prevalence of ISB rocks with Zr/Hf ratios lower than the modelled perovskite source implies that a perovskite cumulate source is not sufficiently depleted to account for this geochemical feature. In fact, this issue also exists for many other geochemical discriminants, such as Th/La, Hf/Sm or Th/Nb, that are all lower in mantle-derived rocks from the Isua region in comparison to the modelled perovskite cumulate origin (Extended Data Fig.
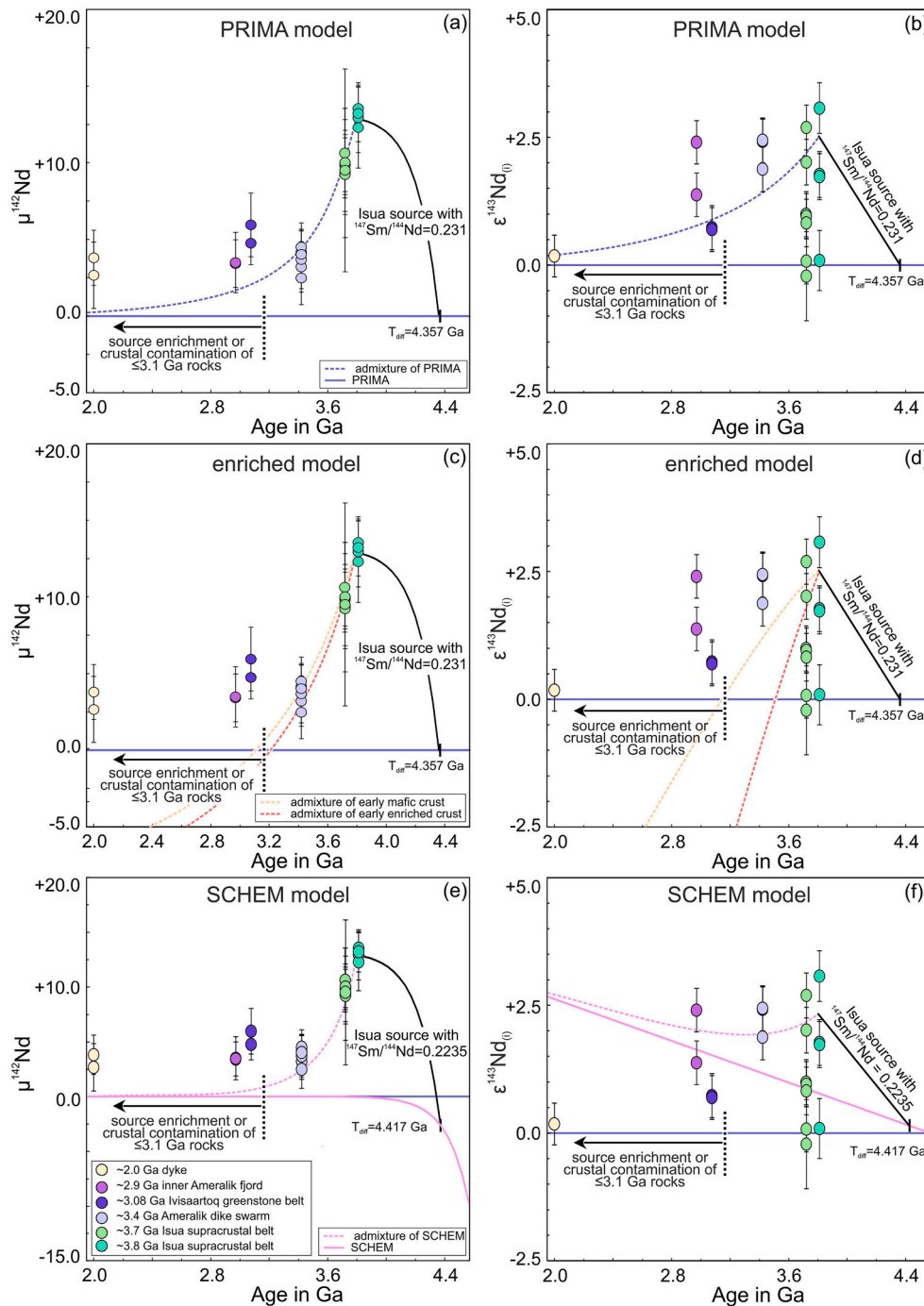

Fig. 6. Coupled $^{142,143}Nd/^{144}Nd$ evolution of the different mantle domains covered in this study over time. Shown are the evolution lines of the depleted Isua mantle source by assuming it was replenished with different bulk Earth compositions. In a) $\mu^{142}Nd$ and b) $\varepsilon^{143}Nd_{(i)}$ values are explained by replenishing the Isua source with primitive mantle material (PRIMA). In c) $\mu^{142}Nd$ and d) $\varepsilon^{143}Nd_{(i)}$ values are explained by replenishing the Isua source with early enriched crust. For this crust we used Nd isotope data from the Ukaliq supracrustal belt (O'Neil et al., 2008) since this material represents the most enriched endmember composition (Fig. 5). For the mafic crust, we used the chemical composition of sample PC282 and for an enriched crust we have used the chemical composition of sample PC286 from (O'Neil et al., 2008). In e) $\mu^{142}Nd$ and f) $\varepsilon^{143}Nd_{(i)}$ values are explained by replenishing the Isua source with superchondritic Earth Material (SCHEM) (Caro and Bourdon, 2010). Isotope ompositions of the different reservoirs over time are given in the Appendix. For our modelling approach, the Isua mantle was replenished with 17% primitive mantle (PRIMA), 0.8% mafic crust, 0.4% felsic crust or 30% of SCHEM material over 100 Ma increments, all assumed to have a bulk Earth $^{142}Nd/^{144}Nd$ composition ($\mu^{142}Nd = 0$) at 3.8 Ga. In the SCHEM model, we assumed a more recently determined $^{142}Nd/^{144}Nd$ difference between Earth and enstatite chondrites of ca. -10 ppm (Saji et al., 2020) and based on that we re-determined the corresponding $^{147}Sm/^{144}Nd$ ratio of SCHEM to be 0.2025. In the superchondritic Earth model, a 2-stage evolution is assumed. The first differentiation lead to a superchondritic BSE that is responsible for the evolution of BSE from $\mu^{142}Nd = -10$ towards $\mu^{142}Nd = 0$. The second differentiation at 4.390 Ga, as constrained here (Fig. 5b), is responsible for the elevated $\mu^{142}Nd$ compositions found in Isua rocks and a consequence of melt extraction from the mantle. However, at 4.390 Ga the $^{142}Nd/^{144}Nd$ composition of BSE is still decreased by ~2.5 ppm in the SCHEM model due to incomplete decay of ^{146}Sm. This issue is compensated by using a slightly higher $^{147}Sm/^{144}Nd$ ratio for the Isua source (see also Table 1 for modelling parameters). For $\mu^{142}Nd$, errors are the same as in Fig. 3 and for $\varepsilon^{143}Nd_{(i)}$, errors depict the propagated errors including uncertainties on parent/ daughter ratios, crystallization age and our external reproducibility of ± 0.4 ε-units on $^{143}Nd/^{144}Nd$ isotope ratios.

4). Since some of the aforementioned element ratios increase further during partial melting or fractional crystallization, perovskite cumulate sources cannot account for the relatively low Th/La, Hf/Sm, La/Sm or Th/Nb ratios present in rocks from the Isua area. Notably, when considering that a subduction overprint (as proposed for the Isua area) typically leads to the fractionation of HFSE (Polat et al., 2002; Hoffmann et al., 2010; van de Löcht et al., 2020), the already present negative Nb—Ta anomalies in a perovskite-related mantle source would be expected to become even larger. This would cause the already unrealistically high Th/Nb ratios to become even higher, which is even more difficult to reconcile with the observed trace element patterns (Extended data Figs. 4 and 5). Therefore, trace element compositions rather argue that mantle depletion as a consequence of simple melt extraction seems more likely to account for the depleted Isua source.

(2) Most importantly, if the observed variability of $\varepsilon^{143}Nd_{(i)}$ values present in ~3.72 and ~3.8 Ga rocks were explained in a single stage perovskite model with varying Ca:Mg perovskite proportions, samples with higher $\varepsilon^{143}Nd_{(i)}$ would also be expected to have the highest $\mu^{142}Nd$ values (cf., Caro et al., 2005; Hoffmann et al., 2011b), an observation that is not found in our dataset nor in previous publications (e.g., Saji et al., 2018). Instead, mantle-derived rocks of the same age show a decoupling of $\mu^{142}Nd$ and $\varepsilon^{143}Nd_{(i)}$ values, with $\mu^{142}Nd$ values remaining constant at variable $\varepsilon^{143}Nd_{(i)}$ values (Figs. 5 and 6). We therefore conclude that a perovskite cumulate related origin cannot explain combined $\varepsilon Hf_{(i)}$- $\varepsilon^{143}Nd_{(i)}$- $\mu^{142}Nd$ patterns and trace element systematics of Isua rocks.

Alternative scenarios that considered the complementary (enriched) reservoir that remained after perovskite cumulate crystallization (cf. Puchtel et al., 2016) also do not fit the trace element compositions and isotope patterns observed in the Isua region. Such a reservoir would have subchondritic Sm/Nd ratios, which will have produced time-integrated negative $\mu^{142}Nd$ and $\varepsilon^{143}Nd_{(i)}$ values over time. However, mixing in such a geochemically complementary reservoir to the Isua mantle source is inconsistent with observational constraints from the Isua area (Bennett et al., 1993; Moorbath et al., 1997; Boyet and Carlson, 2005; Caro et al., 2006; Hoffmann et al., 2010; Hoffmann et al., 2011b; Rizo et al., 2011; Hoffmann et al., 2012; Rizo et al., 2012; Hoffmann et al., 2014; Rizo et al., 2016; van de Löcht et al., 2020). Furthermore, due to the high partition coefficients for Th within Ca-Pv (D_{Th} = 8 to 18) (Corgne et al., 2005), Th will be strongly sequestered into the Pv-cumulates, leaving behind a Th-depleted complementary reservoir, also contradicting trace element observations from ~3.8 to ~3.7 Ga mantle-derived rocks from the Isua region (Polat et al., 2002; Polat and Hofmann, 2003; Jenner et al., 2009; Hoffmann et al., 2010; Hoffmann et al., 2011b; Tusch et al., 2019; van de Löcht et al., 2020). Considering the trace element and isotope constraints discussed above, we therefore conclude that a perovskite-related origin for the geochemical patterns in Eoarchean rocks from Isua is not supported by the available data.

5.5. Late-stage metamorphism

Previous studies suggested partial open-system behavior of the ^{147}Sm—^{143}Nd system during late-stage metamorphism (e.g., Moorbath et al., 1997; Rizo et al., 2011). Such a post-magmatic overprint could explain the high scatter of $\varepsilon^{143}Nd_{(i)}$ values in previous datasets and erroneous ^{147}Sm—^{143}Nd age regressions. Since Lu—Hf and Sm—Nd exhibit a different mobility during post-magmatic alteration, this process might be responsible for decoupled ^{143}Nd—^{176}Hf systematics. Post-magmatic alteration (≤3.72 Ga) might also explain invariant ^{142}Nd isotope compositions (Fig. 5) at highly variable initial ^{143}Nd compositions (see also Moorbath et al. (1997)) as ^{146}Sm went functionally extinct by the end of the Hadean. Other studies have used the $^{143}Nd/^{144}Nd$ intercept of whole rock isochrons to determine initial $\varepsilon^{143}Nd$ values (Moorbath et al., 1997; Rizo et al., 2011), however, in that case the intercept is mainly controlled by samples with the lowest Sm/Nd ratio, which are commonly TTGs that often have lower $\varepsilon^{143}Nd_{(i)}$

values compared to mantle-derived rocks. Furthermore, in case of magma mixing, whole rock isochrons might become too steep, causing too low intercepts at $^{143}Nd/^{144}Nd$. To minimize the above mentioned effects, we have only considered least altered samples from previous studies (Hoffmann et al., 2010; Hoffmann et al., 2011b; van de Löcht et al., 2020). This includes samples that have preserved whole rock ^{147}Sm—^{143}Nd and ^{176}Lu—^{176}Hf errorchron relationships that are in good agreement with an Eoarchean emplacement age, arguing against a large-scale overprint in these samples (Extended Fig. 6). Although this does not fully rule out any late-stage alteration for individual samples, it demonstrates that the majority of samples must have preserved its pristine Hf and Nd isotope composition. Notably, our Isua sample selection shows a significantly lower scatter of initial $\varepsilon^{143}Nd_{(i)}$ values (-0.2 ± 0.9 to $+3.1 \pm 0.5$) compared to those previously reported (Moorbath et al., 1997; Rizo et al., 2011), with the most radiogenic initial $\varepsilon^{143}Nd_{(i)}$ values of our samples being in good agreement with the previously postulated $\varepsilon^{143}Nd_{(i)}$ composition of the Isua mantle source (Moorbath et al., 1997; Bennett et al., 2007). This rather precludes late stage alteration of the Sm—Nd systematics within our set of samples.

5.6. Source enrichment in a subduction zone-like setting

To explain why some of our samples display a tendency towards lower $\varepsilon^{143}Nd_{(i)}$ values another process therefore needs to be considered. In this regard, a subduction zone-like setting as postulated for the Isua area (e.g., Polat et al., 2002; Polat and Hofmann, 2003; Nutman et al., 2007; Jenner et al., 2009; Hoffmann et al., 2010; Hoffmann et al., 2011b; Hoffmann et al., 2012; van de Löcht et al., 2020) offers a viable explanation here. Influx of older recycled material in a subduction zone-like setting (e.g. slab melt addition, mantle metasomatism) can introduce components with more unradiogenic ^{143}Nd compositions to Nd in the Isua mantle source, in line with previous platinum group element constraints on refertilization processes (van de Löcht et al., 2018) and enriched trace element patterns in mafic rocks from Isua (Polat et al., 2002; Polat and Hofmann, 2003; Hoffmann et al., 2010; Hoffmann et al., 2011b; van de Löcht et al., 2018; Tusch et al., 2019). Previous models by van de Löcht et al. (2020) have shown that the incompatible trace element data can be explained by mixing adakitic melts with a depleted upper mantle. This would also be generally in line with a more unradiogenic ^{143}Nd composition of an older recycled component. Our $^{142}Nd/^{144}Nd$ isotope data can place new constraints on the precursor history of the putative Isua source contaminant. Assuming that our samples were affected by source processes to different degrees (van de Löcht et al., 2018), near identical $\mu^{142}Nd$ values in 3.8 Ga old rocks from the Isua area imply that the contaminant and the Isua mantle must have had near identical ^{142}Nd compositions. This implies that both share a common source that underwent the same 4.42 Ga differentiation event (Fig. 5c). Subsequent differentiation that created the enriched component must have had occurred after ^{146}Sm went functionally extinct (<4.0 Ga) to explain the decoupling of ^{143}Nd and ^{142}Nd. We therefore argue that the trace element and Hf—Nd isotope systematics for the northern and southern terrane are rather explained by a complex subduction-like setting for the ISB, involving an ancient depleted Isua mantle source which experienced previous melt extraction that was overprinted by a more enriched component (Polat et al., 2002; Hoffmann et al., 2010; Hoffmann et al., 2011b; van de Löcht et al., 2020). Considering our favored $^{142,143}Nd$ model age of 4.390 Ga (Fig. 5c) and a $\mu^{142}Nd$ excess of $\sim +13$ ppm in ~3.8 Ga rocks, $^{147}Sm/^{144}Nd$ ratios ≥0.22 are required to reproduce the isotope compositions of the pristine Isua mantle source (Fig. 6, Table 1). At ~3.7 to ~3.8 Ga, this is equivalent to an $\varepsilon^{143}Nd$ of $\geq +1.8$, meaning that any $\varepsilon^{143}Nd$ significantly lower than this value rather likely reflects the increased influence of an enriched component.

Magmatic mixing of isotopically heterogeneous components would also affect long-lived ^{176}Lu—^{176}Hf and ^{147}Sm—^{143}Nd isochrons rather insignificantly. When assuming an enriched component with a

Table 1

Modelling parameters used to calculate the adjusted Isua mantle source composition for the PRIMA, SCHEM, and crustal replenishment model.

	PRIMA	SCHEM	Mafic crust[1]	TTG crust[1]
$^{147}Sm/^{144}Nd$[1]	0.1960	0.2025[2]	0.1543	0.109
Adjusted time of Isua differentiation[3]	4.330[4]	4.390[3]	4. 330[4]	4. 330[4]
$\varepsilon^{143}Nd_{(i)}$ BSE at time of differentiation[4]	0.0	+0.1	0.0	0.0
$\varepsilon^{143}Nd_{(3.8Ga)}$ admixed reservoir[4]	0.0	+0.8	−3.3	−6.5
$\mu^{142}Nd$ BSE at time of differentiation[4]	0.0	−3.0	−14.5	−16.2
$\mu^{142}Nd$ Isua source at 3.8 Ga	+13	+13	+13	+13
Adopted $^{147}Sm/^{144}Nd_{source}$[5]	0.2357	0.2300	0.2310	0.2310
$\varepsilon^{143}Nd_{(3.8)}$ adjusted Isua source	+2.5	+2.7	+2.5	+2.5

[1] For the mafic and TTG crust samples PC282 and PC286 from the Ukaliq supracrustal belt in the Superior Provinve were taken from O'Neil et al. (2008) and BSE was assumed to be chondritic.

[2] SCHEM from Caro and Bourdon (2010) was recalculated assuming a ~ −10 ppm difference between BSE and the most terrestrial-like chondrites (Saji et al., 2020) in contrast to the originally assumed ~20 ppm difference, resulting in lower $^{147}Sm/^{144}Nd$ ratios than previously proposed.

[3] For the SCHEM model, the differentiation age used here is the one calculated in this study (Fig. 5b).

[4] The PRIMA model increasingly conflicts with too old differentiation ages, as it would require lower Sm/Nd ratios to explain accompanying elevated $\mu^{142}Nd$ value at 3.8 Ga (compared to a younger differentiation age), leading to too unradiogenic $\varepsilon^{143}Nd$ isotope compositions in the subsequent evolution of the Isua mantle. Therefore, we have assumed a slightly lower differentiation age of 4.330 Ga for the PRIMA model, that still lies within proposed uncertainty (Fig. 5b).

[5] Our modelling approach relies on three parameters, (I) the Isua differentiation model age, (II) the assumed ^{142}Nd composition in 3.8 Ga Isua mantle rocks, and (III) the $\mu^{142}Nd$ composition of the Isua source at the time of differentiation. In a non-chondritic Earth model, $\varepsilon^{143}Nd$ values of BSE will become increasingly positive over time, whereas $\mu^{142}Nd$ will evolve from an initial $\mu^{142}Nd$ deficit of −10 ppm towards a present-day $\mu^{142}Nd = 0$ (i.e., ~enstatite chondritic composition (see also Fig. 6a 6c and 6e). Therefore, a non-chondritic BSE still had a deficit in its $\mu^{142}Nd$ composition that also needs to be considered here when calculating $^{147}Sm/^{144}Nd_{source}$ ratios. As a consequence of this, the $^{147}Sm/^{144}Nd_{source}$ ratio of the Isua source differs slightly in all models.

$^{147}Sm/^{144}Nd$ of 0.10 and a depleted component with a $^{147}Sm/^{144}Nd$ of 0.23 and a $^{143}Nd/^{144}Nd$ composition that was ~1 $\varepsilon^{143}Nd$-unit higher than that of the enriched component, the mixing of both components would create a slope in a $^{147}Sm/^{144}Nd$ vs. $^{143}Nd/^{144}Nd$ space that would correspond to an inferred isochron age that is ~50 Ma higher. Considering, that the ~3.8 and ~ 3.7 Ga terranes both do not have uniform crystallization ages, but rather display a spread in their crystallization ages, it remains ambiguous if this effect would be detectable on a whole rock isochron approach or not. Assuming an uncertainty of one $\varepsilon^{143}Nd$-unit on the initial $\varepsilon^{143}Nd$ due to magma mixing, the calculated ^{142}Nd—^{143}Nd differentiation model approach, would be incorrect by ~45 Ma. This would still be within the errors when using mean values for individual sample localities (Fig. 5b) but strongly outlines the underestimation of errors when using individual samples (Figs. 5a).

5.7. Neodymium isotope evolution of the Isua mantle source through time

Anomalous $^{142}Nd/^{144}Nd$ isotope compositions for Eoarchean rocks from SW-Greenland have been reported by several studies (e.g., Harper and Jacobsen, 1992; Caro et al., 2003; Boyet and Carlson, 2006; Caro et al., 2006; Bennett et al., 2007; Rizo et al., 2011; Rizo et al., 2012; Rizo et al., 2016; Morino et al., 2017; Saji et al., 2018). There is a broad consensus that these ^{142}Nd compositions reflect Hadean silicate differentiation and that the magnitude and frequency of ^{142}Nd anomalies have drastically decreased during the Archean (e.g., Boyet and Carlson, 2006; Caro et al., 2006; Bennett et al., 2007). However, the processes responsible and the reservoirs involved remain poorly understood. In this regard, our study can place new constraints providing new insights into early geodynamic processes.

Previous studies used global ^{142}Nd datasets to infer the timescales at which ^{142}Nd anomalies have disappeared (Carlson and Boyet, 2008; Rizo et al., 2012; Saji et al., 2018; Schneider et al., 2018). However, such conclusions on global mantle homogenization timescales are oversimplified and do not consider that different cratons are linked to distinct geodynamic settings. Instead, the decrease of ^{142}Nd anomalies found in Isua does not necessarily have to reflect one globally driven event but could operate rather locally (Bennett et al., 2007; Morino et al., 2017; Tusch et al., 2021). For example, the ~3.4 Ga Ameralik dikes show clearly resolvable $\mu^{142}Nd$ excesses (Saji et al., 2018) (Fig. 2),

whereas even older 3.5 Ga rocks from the Pilbara Craton already show modern day like $\mu^{142}Nd$ values (Archer et al., 2019; Murphy et al., 2021). This either implies that the ~4.42 Ga differentiation signature in Isua is only of local significance, or, alternatively, that subsequent mantle refertilization processes may have operated heterogeneously and locally different. Therefore, we avoid a comparison at a global scale and only focus on rocks from the IGC and associated greenstone belts (Fig. 6).

To better understand the $^{142}Nd/^{144}Nd$ isotope mantle evolution over time, we have only considered the least contaminated metavolcanic rocks from the Isua area. Considering a subduction zone-like environment as proposed for the Isua region (e.g., Nutman et al., 1999; Polat et al., 2002; Polat and Hofmann, 2003; Nutman et al., 2007; Jenner et al., 2009; Hoffmann et al., 2010; Hoffmann et al., 2011b; Hoffmann et al., 2012; van de Löcht et al., 2020), it needs to be evaluated if the ^{142}Nd systematics can be regarded as reflecting an uncontaminated mantle signal. Recent studies have identified 3.8 Ga Isua peridotites that were variably affected by metasomatism (van de Löcht et al., 2018; van de Löcht et al., 2020). Of these, we have analyzed two samples that are representative of the least metasomatized (sample 10–27) and highly metasomatized (sample 10–34) Isua mantle. As shown in Fig. 2a, both ~3.8 Ga samples display identical $\mu^{142}Nd$ values. This implies that the refertilizing agent must have had $\mu^{142}Nd$ compositions similar to that of the uncontaminated depleted Isua mantle. Therefore, although contaminated, the ^{142}Nd isotope composition of 3.7–3.8 Ga subduction zone-like related rocks from the Isua area can still be used to place new constraints on mantle homogenization processes. The younger ~3.4 Ga Ameralik dike samples analyzed here have slightly depleted LREE compositions (La/Sm = 1.34 to 1.46) and also reveal depleted Th/La$_{PM}$ ratios (0.654 to 0.865) (Tusch et al., 2019). We therefore conclude that the $\mu^{142}Nd$ values of the Mesoarchean Ameralik dikes were not significantly affected by an enriched component and reflect the ambient Isua mantle (see also Saji et al. (2018) who reached an identical conclusion).

All ≤3.1 Ga samples from the Ivisaartoq greenstone belt and the inner Ameralik fjord region analyzed here also show elevated $\mu^{142}Nd$ compositions between +5.9 ± 2.1 and 3.4 ± 1.6. These samples have enriched trace element characteristics (Th/La = 1.01 to 1.58; La/Sm = 1.78 to 3.15) and fairly unradiogenic $\varepsilon^{143}Nd_{(i)}$ values (+0.7 ± 0.4 to +2.4 ± 0.4). Therefore, it has been concluded that they have formed in

geological settings where an older, enriched component was involved (Szilas et al., 2015a; Szilas et al., 2016). Considering that the decrease of $\mu^{142}Nd$ values between the oldest rocks of the IGC at ~3.8 Ga and ~ 3.4 Ga Ameralik dikes (Nutman et al., 2004; Rizo et al., 2012) argues for rather rapid homogenization rates (Fig. 6), we would not expect resolvable mantle-related $\mu^{142}Nd$ anomalies in these younger (Meso-archean) rocks. In some of the samples from the inner Ameralik fjord region, Szilas et al. (2015b) have observed striking similarities of Hf—Nd isotope patterns with those of Isua boninites (Hoffmann et al., 2010). Therefore, it is rather likely that samples from the inner Ameralik fjord region mainly inherited their elevated ^{142}Nd isotope composition from reworking of older IGC crustal fragments. Considering a close genetic relationship between the inner Ameralik fjord region and contemporaneous subduction-related greenstone belts in SW Greenland (Szilas, 2018), we draw similar conclusions for the Ivisaartoq greenstone belt where older enriched crust with positive $\mu^{142}Nd$ values must have been admixed to these rocks. Since this refertilization process appears to delay the homogenization of anomalous $^{142}Nd/^{144}Nd$ compositions with a present-day mantle composition, we do not consider these rocks to straightforwardly constrain mantle homogenization processes. For the slightly elevated $\mu^{142}Nd$ composition and unradiogenic $\varepsilon^{143}Nd_{(i)}$ values in the 2.0 Ga Proterozoic dike, it is also possible that crustal contamination occurred. This would also be in line with ^{142}Nd isotope evidence from the Hudson Bay terrane, NE Canada, where evidence for the long preservation of early crust was observed (O'Neil and Carlson, 2017).

To explain the rapid decrease in ^{142}Nd excesses from ~3.8 to ~3.4 Ga in Isua mantle-derived rocks, we have conducted coupled $^{142,143}Nd/^{144}Nd$ isotope and trace element modelling (Table 1, Figs. 6 and 7). For $^{146}Sm—^{142}Nd$ isotope modelling, we have assumed a solar system initial $^{146}Sm/^{144}Sm$ ratio of 0.00830 and used a ^{146}Sm half-life of 103 Ma (Friedman et al., 1966; Meissner et al., 1987; Fang et al., 2022). Since the $^{142}Nd/^{144}Nd$ compositions of ~3.8 to ~3.4 Ga Isua mantle-derived rocks decrease over time, we assume that another component must have replenished the depleted Isua mantle. To account for the decrease of $^{142}Nd/^{144}Nd$ compositions between 3.8 and 3.4 Ga, we assume that the replenishing component must also had a $\mu^{142}Nd$ excess lower than that of the ancient depleted Isua mantle source. Therefore, it seems unlikely that sedimentary influx within a subduction zone-like setting was responsible for decreasing $\mu^{142}Nd$ values, since ~3.7 to ~3.8 Ga Isua sediments were shown to have identical $^{142}Nd/^{144}Nd$ compositions as the mantle derived rocks (Caro et al., 2003). Replenishing the Isua source with a complementary enriched material from the same differentiation event (negative $\mu^{142}Nd$ and $\varepsilon^{143}Nd$) (e.g., Rosas and Korenaga, 2018) is also not possible, because 3.4 Ga Ameralik dike samples are characterized by rather depleted than enriched trace element characteristics. This gets evident from trace element ratios that are highly susceptible to the interaction with an enriched component (such as Th/Nb or La/Sm) that are all lower than that of the primitive mantle (Palme and O'Neill, 2013), arguing against the interaction with an enriched component. This is also in line with $^{142,143}Nd$ isotope modelling, that is difficult to reconcile with the admixture of an enriched crustal component to the Isua source (Fig. 6 c-d). Therefore, it seems more likely that bulk silicate Earth material with $\mu^{142}Nd$ near the present-day value (zero) progressively diluted the depleted Isua mantle source. This implies that our inferred ~4.42 Ga differentiation event did not occur globally, but some proportions of the bulk silicate Earth remained unfractionated (Bennett et al., 2007).

Regarding the ongoing debate whether the bulk silicate Earth is chondritic or not (Boyet and Carlson, 2006; O'Neill and Palme, 2008; Caro and Bourdon, 2010; Burkhardt et al., 2016; Boyet et al., 2018), we consider two individual scenarios, with different assumptions for the accessible bulk Earth composition, including a primitive mantle (PRIMA) (Palme and O'Neill, 2013), or a superchondritic Earth model
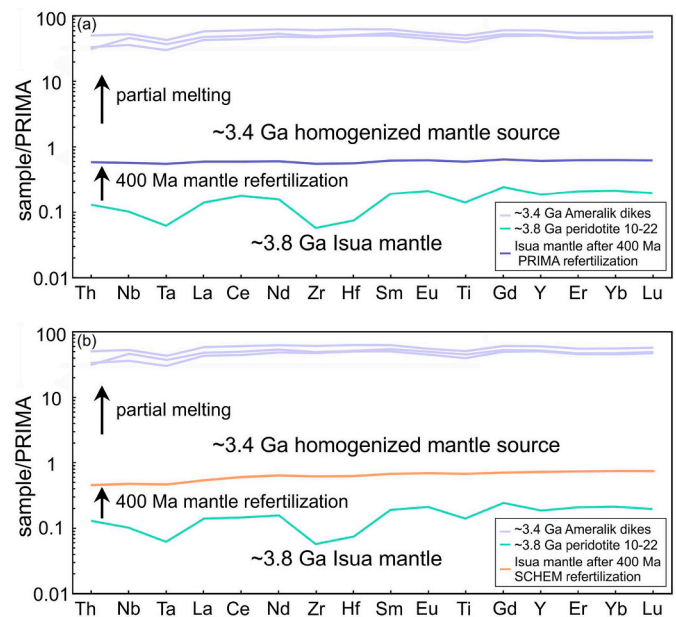

Fig. 7. Evolution of trace element compositions for the same model as in Fig. 6. Shown is the trace element composition of the homogenized mantle source at 3.4 Ga after being replenished for 400 Ma with BSE material (i.e. PRIMA in a) or SCHEM in b)). At 3.4 Ga, the homogenized mantle source is flat without having any Zr—Hf or Nb—Ta anomalies. The modelled trace element pattern of our homogenized mantle source therefore can well explain the flat trace element patterns of contemporaneous 3.4 Ga Ameralik dikes (shown for comparison). For the Isua mantle source, the composition of a mantle peridotite type 1 (sample 10–22) was assumed to be representative of the mantle beneath the Isua region at 3.8 Ga (van de Löcht et al., 2020). For the trace element composition of SCHEM, the superchondritic BSE composition of O'Neill and Palme (2008) was used and expanded for further trace elements (Nb, Ta, Ce, Pr, Zr, Sm, Eu, Ti, Gd, Tb, Dy, Y, Er, Yb), using their stated modelling parameters. Trace element data for the ~3.4 Ga Ameralik dikes are taken from Tusch et al., (2019) for comparison with our modelled near-contemporaneous mantle source. Trace element compositions are listed in Appendix. Since replenishing the Isua source with enriched material cannot explain the coupled $\mu^{142}Nd$ and $\varepsilon^{143}Nd_{(i)}$ values (Fig. 6), we have not conducted trace element modelling for this model.

(SCHEM) composition (Caro and Bourdon, 2010). The difference between the chondritic PRIMA model and the superchondritic SCHEM models is that the latter one assumes an initial $^{142}Nd/^{144}Nd$ composition below the terrestrial value at superchondritic $^{147}Sm/^{144}Nd$ ratios (see Table 1 for adjusted BSE compositions and modelling parameters). Due to its elevated $^{147}Sm/^{144}Nd$ ratio, a SCHEM-like BSE will evolve towards a $\mu^{142}Nd = 0$ and slightly positive $\varepsilon^{143}Nd$ over time. In contrast, the chondritic Earth model assumes that Earth has a chondritic $^{147}Sm/^{144}Nd$ ratio and had a $\mu^{142}Nd = 0$ throughout its history. Generally, it is possible to explain the combined $^{142,143}Nd$ constraints on the ancient depletion event of the Isua mantle and its subsequent replenishment by considering both scenarios.

In our model, we have refertilized the depleted Isua source by admixing 17% PRIMA or 30% SCHEM material to the Isua source in incremental steps every 100 Ma (Fig. 6-8, Table 1) to simulate a progressive interaction between the depleted Isua mantle and undifferentiated bulk silicate Earth material. Between 3.8 and 3.4 Ga, both replenishment models will cause a decrease of $^{142}Nd/^{144}Nd$ anomalies that converge towards $\mu^{142}Nd = 0$. Between 3.8 and 3.4 Ga, $\varepsilon^{143}Nd$ decrease slightly in all three scenarios, in accord with our observations.

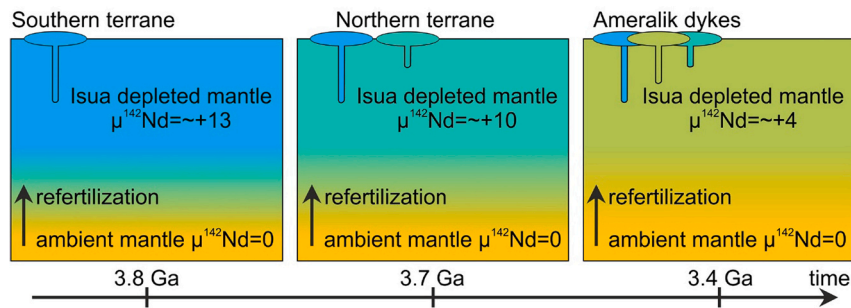In a next step, we further validated our model from a trace element

Fig. 8. Schematic model illustration the homogenization of $^{142}Nd/^{144}Nd$ anomalies in the Isua mantle region. A differentiation event at ~4.42 Ga created a depleted reservoir that evolved towards $\mu^{142}Nd$ values of +13 at 3.8 Ga. This depleted mantle beneath the Isua region was progressively diluted by admixing primordial mantle material that was not involved in this previous differentiation event.

perspective. For consistency, we applied the same modelling parameters as for our isotope modelling approach. In their study, van de Löcht et al. (2020) described a group of mantle peridotites that were least affected by metasomatizing agents and interpreted them as representatives for the pristine Isua mantle (their Group 1). From this group, we used sample 10–22 as starting composition for our replenishment model. Following our model, the admixture of PRIMA or SCHEM to the Isua mantle will flatten the incompatible trace element pattern and erase Ti, Zr—Hf and Nb—Ta anomalies present in the depleted 3.8 to 3.7 Ga Isua mantle (Fig. 7). Although Caro and Bourdon (2010) have not provided trace element compositions for SCHEM, a hypothetical superchondritic terrestrial composition was previously calculated by O'Neill and Palme (2008) that are in line with previous trace element constraints on a non-chondritic terrestrial composition (Carlson and Boyet, 2008; Jackson and Jellinek, 2013). Based on their modelling parameters, we have extended their model for further trace elements (Nb, Ta, Ce, Pr, Zr, Sm, Eu, Ti, Gd, Tb, Dy, Y, Er, Yb) and assumed this composition as representative for the SCHEM replenishment model. Generally, at 3.4 Ga the PRIMA and SCHEM replenished mantle both exhibit nearly flat incompatible trace element patterns without significant Ti, Zr—Hf, and Nb—Ta anomalies. Both trace element characteristics can well account for the source of near-contemporaneous Ameralik dykes (Fig. 7).

Although both models yield near-identical results at ~3.4 Ga, there is one striking difference between the primitive and the superchondritic model. The superchondritic model will evolve towards elevated $\varepsilon^{143}Nd$ values over time whereas $\varepsilon^{143}Nd$ values in the PRIMA model will converge towards 0. At ~3.3 to 3.2 Ga, the chondritic and the superchondritic model will both have developed towards clearly resolvable $\varepsilon^{143}Nd$ values. Since there are Ameralik dikes as young as 3.265 Ga (Nutman et al., 2004), these rocks would be able to provide further evidence for discriminating between both models.

6. Conclusions

In this study, we have developed a new analytical protocol to conduct high precision mass-independent Nd isotope measurements, including radiogenic ^{142}Nd and ^{143}Nd. This method was verified by confirming previous $^{142}Nd/^{144}Nd$ results for samples from the well-characterized Isua region in SW Greenland and by measuring various mixtures of a well-characterized ^{142}Nd excess-bearing TTG that was doped with different amounts of reference material BHVO-2. Our intermediate precision (± 1.4 ppm; 2rsd) is defined by 23 analysis of a La Palma basalt (LP-1) that each typically comprise 10–12 single measurements, bracketed by a JNdi-1 reference standard. Our intermediate precision demonstrates that we are able to resolve anomalies at the

lowest ppm level. In conjunction with previous literature data for 3.8–3.7 Ga old rocks from the North Atlantic Craton and the East Superior Province, we infer a $^{142,143}Nd/^{144}Nd$ differentiation model age of $4.390^{+0.045}_{-0.060}$ Ga, in excellent agreement with previous estimates.

Our study is the first revealing a statistically significant difference of $^{142}Nd/^{144}Nd$ compositions in ~3.72 Ga and ~ 3.8 Ga Isua rocks. While ~3.8 Ga mafic-ultramafic rocks have an average $\mu^{142}Nd$ value of +13.0 ± 1.1, ~3.72 Ga mafic-ultramafic rocks show resolvably lower $\mu^{142}Nd$ values of +9.8 ± 1.0. Analysis of ~3.4 Ga Ameralik dikes reveal even lower $\mu^{142}Nd$ values with an average of +3.8 ± 1.1. The decrease of ^{142}Nd anomalies in the Isua area between 3.8 and 3.4 Ga is best explained by progressive admixture of BSE material to the depleted Isua mantle. With respect to the ongoing debate whether Earth is chondritic or not, our model demonstrates that this can be achieved by both primitive or superchondritic BSE material. In addition to the previously described $\varepsilon^{143}Nd$-εHf decoupling, ISB rocks are also exhibit a decoupling of $^{142,143}Nd/^{144}Nd$ compositions by having homogeneous $\mu^{142}Nd$ values but more variable $\varepsilon^{143}Nd_{(i)}$ values. This feature is best explained by supply of material with similar $^{142}Nd/^{144}Nd$ but different $^{143}Nd/^{144}Nd$ systematics to the mantle via recycling processes that may be comparable to modern-style subduction environments. Younger volcanic rocks from Mesoarchean terranes reveal higher ^{142}Nd compositions than expected from our replenishment model. This observation can be best explained by reworking older Isua crust that provided recycled material with anomalous ^{142}Nd compositions to the mantle.

Declaration of Competing Interest
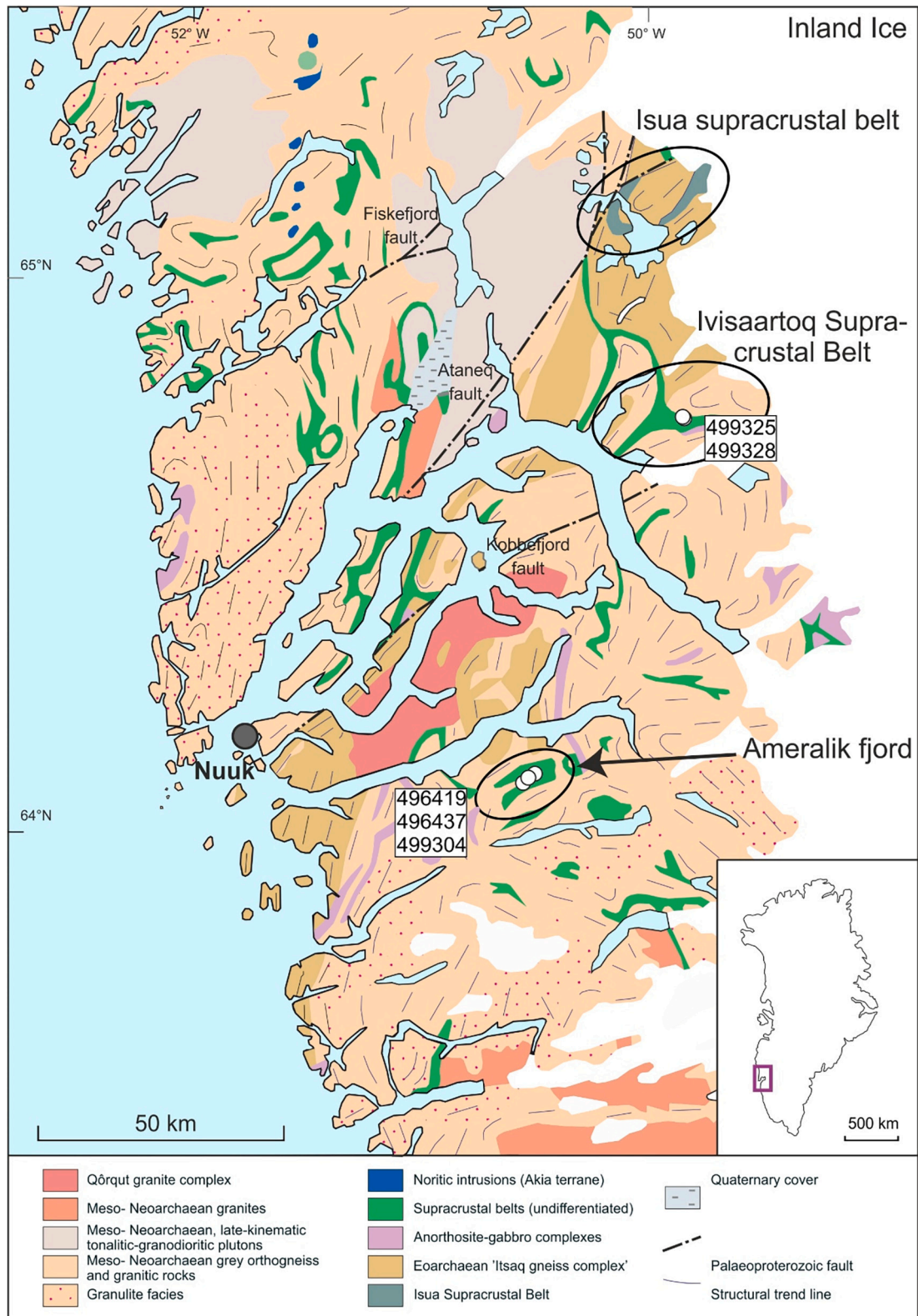
The authors declare no conflicts of interest.

Data availability

Data will be made available on request.

Appendix

Extended Data Fig. 1. Geological map of the Nuuk region, highlighting our studied areas. Shown are the sample locations for samples from the Ameralik Fjord region and the Ivisaartoq Supracrustal Belt. The map is modified after Szilas et al., (2015b) and based on work by the Geological Survey of Denmark and Greenland.
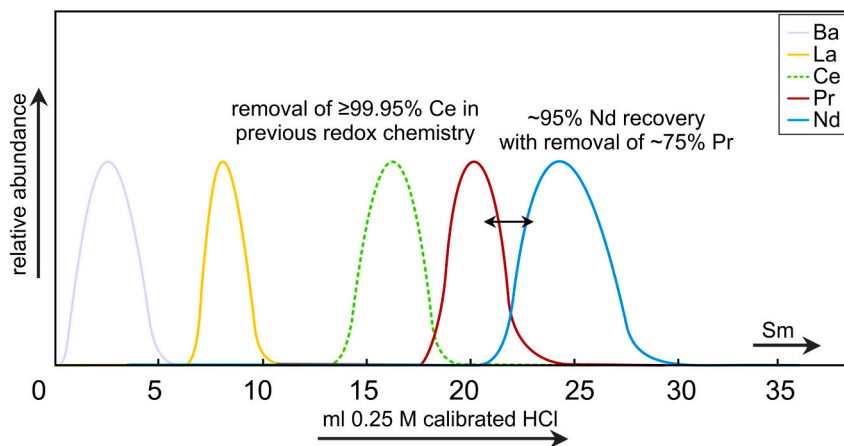
Extended Data Table 1

| Stage	Reagent	Volumes [ml]
I Separation of HFSE and matrix		
Column I (15 ml BioRad AG 50 W-X-8)		
Preconditioning	1 M HCl - 0.3% H_2O_2	2×20
Load, HFSE & Ti	1 M HCl - 0.3% H_2O_2	20
Elute HFSE & Ti	1 M HCl - 0.3% H_2O_2	15
Elute major element matrix	1.8 M HCl	80
Collect REE, Sr and Ba	6 M HCl	100
II Separation of LREE from remaining matrix and HREE		
Column II (6 ml BioRad AG 50 W-X-8)		
Preconditioning	2.5 M HCl	2×10
Load, elute remaining matrix and HREE	2.5 M HCl	5
Elute remaining matrix and HREE	2.5 M HCl	27
Collect LREE and Ba[a]	6 M HCl	35
III Separation of REE from Ce		
Column III (0.5 ml Ln Spec® resin)		
Preconditioning	10 M HNO_3	4
Preconditioning	10 M HNO_3–20 mM $KBrO_3$	6
Load, elute LREE, Ba and K	10 M HNO_3–20 mM $KBrO_3$	0.5
Elute LREE, Ba and K[a]	10 M HNO_3–20 mM $KBrO_3$	7.5
Elute Ce	10 M HNO_3	2
Elute Ce	H_2O	2
Elute Ce	6 M HCl - 1% H_2O_2	6
IV Separation of LREE and Ba from K		
Column II (6 ml BioRad AG 50 W-X-8)		
Preconditioning	2.5 M HCl	2×10
Load, elute K	2.5 M HCl	5
Elute K	2.5 M HCl	27
Collect LREE and Ba[a]	6 M HCl	35
V Separation of Nd from other LREE and Ba		
Column IV (6 ml 50 μm Ln Spec® resin and 0.4 ml AG ® 1-X8 on top)		
Preconditioning	0.25 calibrated HCl	2×10
Load	0.25 calibrated HCl	0.5
Elute Ba, La, residual Ce and Pr[b]	0.25 calibrated HCl	25
Collect Nd[a]	0.25 calibrated HCl	12

[a]Dry down two times with 80 μl 14 M HNO_3 + 40 μl 30% H_2O_2

[b]For Nd cuts, the last 3–5 ml were collected in 1 ml steps seperately and recombined to ensure best possible Pr—Nd separation with maximum Nd yields

Elution scheme for purifying Nd from rock samples. Modified after Pin and Zalduegui, (1997), Schnabel et al., (2017) and Tusch et al., (2019).


Extended Data Fig. 2. Schematic REE elution (separation step V) on Ln® Spec resin. Protocol is modified after Pin and Zalduegui, (1997).
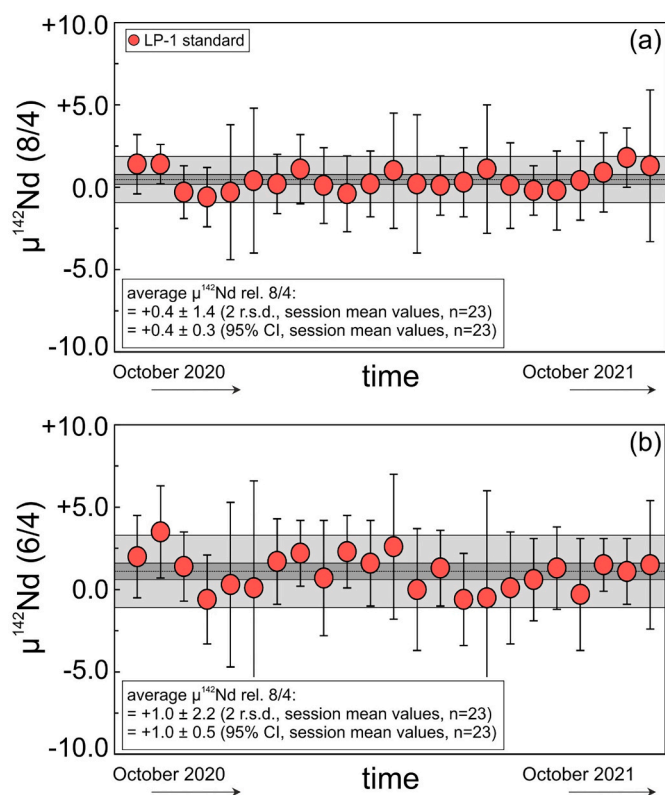
Extended Data Fig. 3. Intermediate precision of 22 multiple measurements for our in-house reference material LP-1, using a) ^{148}Nd/^{144}Nd (8/4) or b) ^{146}Nd/^{144}Nd (6/4) for mass bias correction. The smaller dark grey bars and the larger light grey bars refer to the mean 95% CI and 2 r.s.d. for all multiple measurement values (N typically 10 to 12), respectively. Our intermediate precision of ±1.4 ppm (2rsd) on ^{142}Nd/^{144}Nd (8/4) analysis is considered as minimum error.
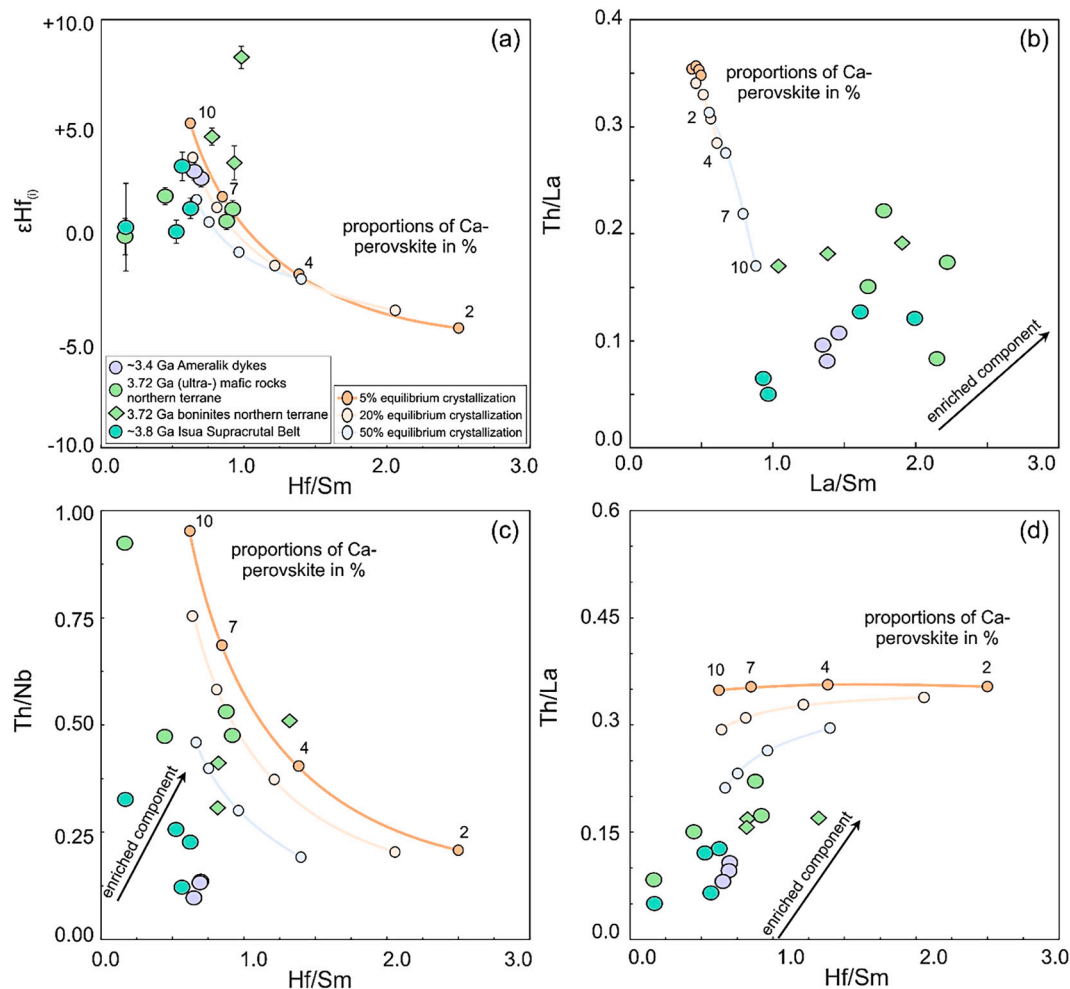
Extended Data Fig. 4. Evaluation whether trace element and isotope characteristics of ~3.8 to ~3.4 Ga Isua rocks can be explained by tapping perovskite cumulates with different degrees of crystallization and variable Ca—Mg perovskite proportions. a) Isua rocks show positive covariations between εHf$_{(i)}$ and Hf/Sm, whereas perovskite cumulates would create inverse correlations. b) Th/La vs. La/Sm, c) Th/Nb vs. Hf/Sm and d) Th/La vs. Hf/Sm reveal that some Isua samples are more depleted (i.e., having lower Th/La, Hf/Sm or Th/Nb ratios) than the modelled perovskite cumulates. Since partial melting increases these ratios, perovskite cumulates are too enriched to be a viable source. Notably, we have modelled Ca—Mg perovskite proportions as previously postulated for the Isua region (Caro et al., 2005; Hoffmann et al., 2011b; Rizo et al., 2011) and assuming a wide range of crystallization degrees (5% to 50%). For εHf$_{(i)}$, errors shown are the propagated errors including the errors on parent/daughter ratios, crystallization age and our external reproducibility of ±0.4 ε-units on ^{176}Hf/^{177}Hf isotope ratios. See Appendix for model parameters. Additional data from previous studies (Polat et al., 2002; Polat and Hofmann, 2003; Hoffmann et al., 2010; Hoffmann et al., 2011b; van de Löcht et al., 2018; Tusch et al., 2019; van de Löcht et al., 2020).
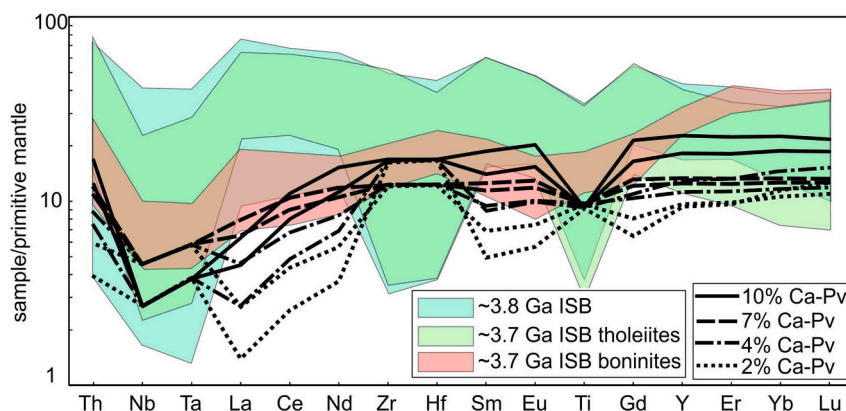
Extended Data Fig. 5. Comparison of observed and modelled trace element pattern, assuming a perovskite-related cumulate origin. Perovskite cumulates would create strong fractionations between REE and HFSE. Please note that fractionation within a subduction-like setting as proposed earlier would lead to even more fractionated HFSE patterns. Modelling parameters are as in Extended Data Fig. 4 but with an emphasis on trace element characteristics. For the different Ca/Mg-perovskite ratios, two lines are always shown, one assuming 5% and the other assuming 50% Pv equilibrium crystallization. See Appendix for detailed model parameters. Shaded trace element data are from previous studies (Polat et al., 2002; Polat and Hofmann, 2003; Hoffmann et al., 2010; Hoffmann et al., 2011b; van de Löcht et al., 2018; Tusch et al., 2019).
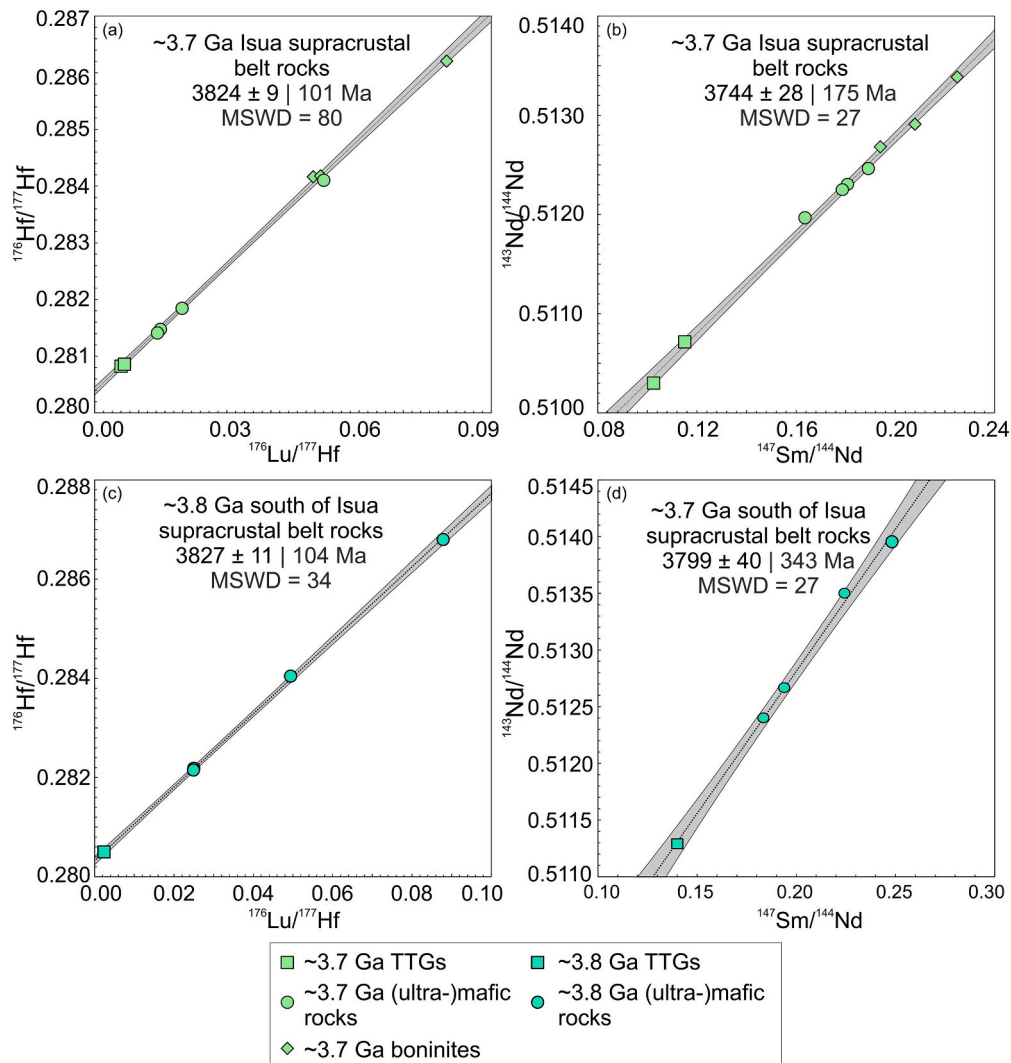
Extended Data Fig. 6. Isochron relationships for Eoarchean rocks from this study. a) $^{176}Lu-^{176}Hf$ isochron for ~3.7 Ga Isua supra crustal belt; b) $^{147}Sm-^{143}Nd$ isochron for ~3.7 Ga Isua supra crustal belt; c) $^{176}Lu-^{176}Hf$ isochron for ~3.8 Ga Isua supra crustal belt and d) $^{147}Sm-^{143}Nd$ isochron for ~3.8 Ga Isua supra crustal belt. The preservation of Eoarchean whole-rock isochrons argues against large-scale open system behavior of $^{147}Sm-^{143}Nd$ and $^{176}Lu-^{176}Hf$ isochron relationships, although the high MSWDs argue for heterogeneous initial radiogenic isotope compositions, possibly linked to magma mixing. Errors are smaller than the symbol sizes. The first error on the ages represents the 2rsd, whereas the second one also considers overdispersion as already indicated by the high MSWDs. Calculated using IsoplotR (Vermeesch, 2018). Long-lived data was taken from previous studies that were analyzed for their ^{142}Nd isotope composition in this study (Hoffmann et al., 2010; Hoffmann et al., 2011b; Hoffmann et al., 2011a; van de Löcht et al., 2018).

Appendix A. Supplementary data

Supplementary data to this article can be found online at https://doi.org/10.1016/j.chemgeo.2022.121141.

References

Allègre, C.J., Manhès, G., Göpel, C., 2008. The major differentiation of the Earth at ~ 4.45 Ga. Earth Planet. Sci. Lett. 267, 386–398.

Amelin, Y., Kamo, S.L., Lee, D.C., 2011. Evolution of early crust in chondritic or nonchondritic Earth inferred from U-Pb and Lu-Hf data for chemically abraded zircon from the Itsaq Gneiss Complex West Greenland. Can. J. Earth Sci. 48, 141–160.

Archer, G.J., Brennecka, G.A., Gleißner, P., Stracke, A., Becker, H., Kleine, T., 2019. Lack of late-accreted material as the origin of 182W excesses in the Archean mantle: evidence from the Pilbara Craton, Western Australia. Earth Planet. Sci. Lett. 528, 115841. Available at: https://doi.org/10.1016/j.epsl.2019.115841.

Bennett, V.C., Nutman, A.P., McCulloch, M.T., 1993. Nd isotopic evidence for transient, highly depleted mantle reservoirs in the early history of the Earth. Earth Planet. Sci. Lett. 119, 299–317.

Bennett, V.C., Brandon, A.D., Nutman, A.P., 2007. Coupled 142Nd-143Nd isotopic evidence for hadean mantle dynamics. Science (80-.) 318, 1907–1910.

Bouvier, A., Vervoort, J.D., Patchett, P.J., 2008. The Lu-Hf and Sm-Nd isotopic composition of CHUR: Constraints from unequilibrated chondrites and implications for the bulk composition of terrestrial planets. Earth Planet. Sci. Lett. 273, 48–57.

Boyet, M., Carlson, R.W., 2005. 142Nd evidence for early (>4.53 Ga) global differentiation of the silicate earth. Science (80) 309, 576–581.

Boyet, M., Carlson, R.W., 2006. A new geochemical model for the Earth's mantle inferred from 146Sm-142Nd systematics. Earth Planet. Sci. Lett. 250, 254–268.

Boyet, M., Blichert-Toft, J., Rosing, M.T., Storey, M., Teoluk, P., Albarède, F., 2003. 142Nd evidence for early Earth differentiation. Earth Planet. Sci. Lett. 214, 427–442.

Boyet, M., Bouvier, A., Frossard, P., Hammouda, T., Garçon, M., Gannoun, A., 2018. Enstatite chondrites EL3 as building blocks for the Earth: the debate over the 146Sm–142Nd systematics. Earth Planet. Sci. Lett. 488, 68–78. Available at: https://doi.org/10.1016/j.epsl.2018.02.004.

Brandon, A.D., Lapen, T.J., Debaille, V., Beard, B.L., Rankenburg, K., Neal, C., 2009. Re-evaluating 142Nd/144Nd in lunar mare basalts with implications for the early evolution and bulk Sm/Nd of the Moon. Geochim. Cosmochim. Acta 73, 6421–6445. Available at: https://doi.org/10.1016/j.gca.2009.07.015.

Budde, G., Burkhardt, C., Kleine, T., 2019. Molybdenum isotopic evidence for the late accretion of outer Solar System material to Earth. Nat. Astron. 3, 736–741.

Burkhardt, C., Borg, L.E., Brennecka, G.A., Shollenberger, Q.R., Dauphas, N., Kleine, T., 2016. A nucleosynthetic origin for the Earth's anomalous 142 Nd composition. Nature 537, 394–398. Available at: https://doi.org/10.1038/nature18956.

Carlson, R.W., Boyet, M., 2008. Composition of the Earth's interior: the importance of early events. Philos. Trans. R Soc. A Math. Phys. Eng. Sci. 366, 4077–4103.

Caro, G., Bourdon, B., 2010. Non-chondritic Sm/Nd ratio in the terrestrial planets: Consequences for the geochemical evolution of the mantle-crust system. Geochim. Cosmochim. Acta 74, 3333–3349. Available at: https://doi.org/10.1016/j.gca.2010.02.025.

Caro, G., Bourdon, B., Birck, J.L., Moorbath, S., 2003. 146Sm-142Nd evidence from Isua metamorphosed sediments for early differentiation of the Earth's mantle. Nature 423, 428–432.

Caro, G., Bourdon, B., Wood, B.J., Corgne, A., 2005. Trace-element fractionation in Hadean mantle generated by melt segregation from a magma ocean. Nature 436, 246–249. https://doi.org/10.1038/nature03827.

Caro, G., Bourdon, B., Birck, J.L., Moorbath, S., 2006. High-precision 142Nd/144Nd measurements in terrestrial rocks: Constraints on the early differentiation of the Earth's mantle. Geochim. Cosmochim. Acta 70, 164–191.

Caro, G., Morino, P., Mojzsis, S.J., Cates, N.L., Bleeker, W., 2017. Sluggish Hadean geodynamics: evidence from coupled 146,147Sm–142,143Nd systematics in Eoarchean supracrustal rocks of the Inukjuak domain (Québec). Earth Planet. Sci. Lett. 457, 23–37.

Cates, N.L., Ziegler, K., Schmitt, A.K., Mojzsis, S.J., Lyon, D., 2013. Reduced, reused and recycled : Detrital zircons define a maximum age for the Eoarchean (ca. 3750–3780 Ma) Nuvvuagittuq Supracrustal Belt, Que. Earth Planet. Sci. Lett. 362, 283–293. Available at: https://doi.org/10.1016/j.epsl.2012.11.054.

Chowdhury, W., Trail, D., Guitreau, M., Bell, E.A., Buettner, J., Mojzsis, S.J., 2020. Geochemical and textural investigations of the Eoarchean Ukaliq supracrustals, Northern Québec (Canada). Lithos 372–373, 105673. Available at: https://doi.org/10.1016/j.lithos.2020.105673.

Corgne, A., Liebske, C., Wood, B.J., Rubie, D.C., Frost, D.J., 2005. Silicate perovskite-melt partitioning of trace elements and geochemical signature of a deep perovskitic reservoir. Geochim. Cosmochim. Acta 69, 485–496.

Crowley, J.L., 2003. U-Pb geochronology of 3810-3630 Ma granitoid rocks south of the Isua greenstone belt, southern West Greenland. Precambrian Res. 126, 235–257.

Debaille, V., O'Neill, C., Brandon, A.D., Haenecour, P., Yin, Q.Z., Mattielli, N., Treiman, A.H., 2013. Stagnant-lid tectonics in early Earth revealed by 142Nd variations in late Archean rocks. Earth Planet. Sci. Lett. 373, 83–92.

Fang, L., Frossard, P., Boyet, M., Bouvier, A., Barrat, J.A., Chaussidon, M., Moynier, F., 2022. Half-life and initial Solar System abundance of 146Sm determined from the oldest andesitic meteorite. Philos. Trans. R. Soc. 119.

Frei, R., Rosing, M.T., Waight, T.E., Ulfbeck, D.G., 2002. Hydrothermal-metasomatic and tectono-metamorphic processes in the Isua supracrustal belt (West Greenland): a multi-isotopic investigation of their effects on the Earth's oldest oceanic crustal sequence. Geochim. Cosmochim. Acta 66, 467–486.

Friedman, A., Milsted, J., Metta, D., Henderson, D., Lerner, J., Harkness, A., 1966. Alpha Decay half lives of 148Gd 150Gd, and 146Sm*. Radiochim. Acta 5, 192–194.

Friend, C., Nutman, A., Baadsgaard, H., Kinny, P., McGregor, V., 1996. Meta-igneous (non-gneissic) tonalites and quartz diorites from an extensive ca. 3800 Ma terrain south of the Isua supracrustal belt, southern west Greenland: constraints on early crust formation. Earth Planet. Sci. Lett. 142, 353–365. Available at: http://www.sciencedirect.com/science/article/pii/0012821X96001185.

Garçon, M., Boyet, M., Carlson, R.W., Horan, M.F., Auclair, D., Mock, T.D., 2018. Factors influencing the precision and accuracy of Nd isotope measurements by thermal ionization mass spectrometry. Chem. Geol. 476, 493–514. Available at: https://doi.org/10.1016/j.chemgeo.2017.12.003.

Guitreau, M., Blichert-Toft, J., Mojzsis, S.J., Roth, A.S.G., Bourdon, B., 2013. A legacy of Hadean silicate differentiation inferred from Hf isotopes in Eoarchean rocks of the Nuvvuagittuq supracrustal belt (Québec, Canada). Earth Planet. Sci. Lett. 362, 171–181.

Harper, C.L., Jacobsen, S.B., 1992. Evidence from coupled 147Sm-143Nd and 146Sm-142Nd systematics for very early (4.5-Gyr) differentiation of the Earth's mantle, 360, 728–732.

Hasenstab, E., Tusch, J., Schnabel, C., Marien, C.S., Van Kranendonk, M.J., Smithies, H., Howard, H., Maier, W.D., Münker, C., 2021. Evolution of the early to late Archean mantle from Hf-Nd-Ce isotope systematics in basalts and komatiites from the Pilbara Craton. Earth Planet. Sci. Lett 553.

Hiess, J., Bennett, V.C., Nutman, A.P., Williams, I.S., 2009. In situ U-Pb, O and Hf isotopic compositions of zircon and olivine from Eoarchaean rocks, West Greenland: New insights to making old crust. Geochim. Cosmochim. Acta 73, 4489–4516. Available at: https://doi.org/10.1016/j.gca.2009.04.019.

Hoffmann, J.E., Wilson, A.H., 2017. The origin of highly radiogenic Hf isotope compositions in 3.33 Ga Commondale komatiite lavas (South Africa). Chem. Geol. 455, 6–21. Available at: https://doi.org/10.1016/j.chemgeo.2016.10.010.

Hoffmann, J.E., Münker, C., Polat, A., König, S., Mezger, K., Rosing, M.T., 2010. Highly depleted Hadean mantle reservoirs in the sources of early Archean arc-like rocks, Isua supracrustal belt, southern West Greenland. Geochim. Cosmochim. Acta 74, 7236–7260.

Hoffmann, J.E., Münker, C., Næraa, T., Rosing, M.T., Herwartz, D., Garbe-Schönberg, D., Svahnberg, H., Mnker, C., Nraa, T., Rosing, M.T., Herwartz, D., Garbe-Schonberg, D., Svahnberg, H., 2011a. Mechanisms of Archean crust formation inferred from high-precision HFSE systematics in TTGs. Geochim. Cosmochim. Acta 75, 4157–4178.

Hoffmann, J.E., Münker, C., Polat, A., Rosing, M.T., Schulz, T., 2011b. The origin of decoupled Hf-Nd isotope compositions in Eoarchean rocks from southern West Greenland. Geochim. Cosmochim. Acta 75, 6610–6628.

Hoffmann, J.E., Svahnberg, H., Piazolo, S., Scherstén, A., Münker, C., 2012. The geodynamic evolution of Mesoarchean anorthosite complexes inferred from the Naajat Kuuat Complex, southern West Greenland. Precambrian Res. 196–197, 149–170. Available at: https://doi.org/10.1016/j.precamres.2011.12.002.

Hoffmann, J.E., Nagel, T.J., Münker, C., Næraa, T., Rosing, M.T., 2014. Constraining the process of Eoarchean TTG formation in the Itsaq Gneiss complex, southern West Greenland. Earth Planet. Sci. Lett. 388, 374–386. Available at: https://doi.org/10.1016/j.epsl.2013.11.050.

Horan, M.F., Carlson, R.W., Walker, R.J., Jackson, M., Garçon, M., Norman, M., 2018. Tracking Hadean processes in modern basalts with 142-Neodymium. Earth Planet. Sci. Lett. 484, 184–191. Available at: https://doi.org/10.1016/j.epsl.2017.12.017.

Hyung, E., Jacobsen, S.B., 2020. The 142Nd/144Nd variations in mantle-derived rocks provide constraints on the stirring rate of the mantle from the Hadean to the present. Proc. Natl. Acad. Sci. U. S. A. 117, 14738–14744.

Hyung, E., Tissot, F.L.H., 2021. Routine high-precision Nd isotope analyses: an optimized chromatographic purification scheme. J. Anal. At. Spectrom 36, 1946–1959. https://doi.org/10.1039/d1ja00169h.

Jackson, M.G., Jellinek, A.M., 2013. Major and trace element composition of the high 3He/ 4He mantle: Implications for the composition of a nonchondritic Earth. Geochemistry Geophys. Geosystems 14, 2954–2976.

Jenner, F.E., Bennett, V.C., Nutman, A.P., Friend, C.R.L., Norman, M.D., Yaxley, G., 2009. Evidence for subduction at 3.8 Ga: Geochemistry of arc-like metabasalts from the southern edge of the Isua Supracrustal Belt. Chem. Geol. 261, 83–98. Available at: https://doi.org/10.1016/j.chemgeo.2009.09.016.

Kamber, B.S., Tomlinson, E.L., 2019. Petrological, mineralogical and geochemical peculiarities of Archaean cratons. Chem. Geol. 511, 123–151.

Kisters, A.F.M., van Hinsberg, V.J., Szilas, K., 2012. Geology of an Archaean accretionary complex - the structural record of burial and return flow in the Tartoq Group of South West Greenland. Precambrian Res. 220–221, 107–122. Available at: https://doi.org/10.1016/j.precamres.2012.07.008.

Marks, N.E., Borg, L.E., Hutcheon, I.D., Jacobsen, B., Clayton, R.N., 2014. Samarium-neodymium chronology and rubidium-strontium systematics of an Allende calcium-aluminum-rich inclusion with implications for 146Sm half-life. Earth Planet. Sci. Lett. 405, 15–24. Available at: https://doi.org/10.1016/j.epsl.2014.08.017.

Meissner, F., Schmidt-Ott, W.D., Ziegeler, L., 1987. Half-Life and alpha-Ray Energy of 146Sm. Zeitschrift für Phys. 174, 171–174.

Moorbath, S., Allaart, J.H., Bridgwater, D., McGregor, V.R., 1977. Rb-Sr ages of early Archean supracrustal rocks and Amitsoq gneisses at Isua. Nature 270, 43–45.

Moorbath, S., Whitehouse, M.J., Kamber, B.S., 1997. Extreme Nd-isotope heterogeneity in the early Archaean - Fact or fiction? Case histories from northern Canada and West Greenland. Chem. Geol. 135, 213–231.

Morino, P., Caro, G., Reisberg, L., Schumacher, A., 2017. Chemical stratification in the post-magma ocean Earth inferred from coupled 146,147Sm–142,143Nd systematics in ultramafic rocks of the Saglek block (3.25–3.9 Ga; northern Labrador, Canada). Earth Planet. Sci. Lett. 463, 136–150. Available at: https://doi.org/10.1016/j.epsl.2017.01.044.

Morino, P., Caro, G., Reisberg, L., 2018. Differentiation mechanisms of the early Hadean mantle: Insights from combined 176Hf-142,143Nd signatures of Archean rocks from the Saglek Block. Geochim. Cosmochim. Acta 240, 43–63.

Mukhopadhyay, S., 2012. Early differentiation and volatile accretion recorded in deep-mantle neon and xenon. Nature 486, 101–104. Available at: https://doi.org/10.1038/nature11141.

Münker, C., Weyer, S., Scherer, E., Mezger, K., 2001. Seperation of high field strength elements (Nb, Ta, Zr, Hf) and Lu from rock samples for MC-IPMS measurements. Geochemistry Geophys. Geosystems 2, 1–19.

Münker, C., Pfänder, J.A., Weyer, S., Büchl, A., Kleine, T., Mezger, K., 2003. Evolution of planetary cores and the Earth-Moon system from Nb/Ta systematics. Science (80) 301, 84–87.

Murphy, D., Rizo, H., O'Neil, J., Hepple, R., Wiemer, D., Kemp, A., Vervoort, J., 2021. Combined Sm-Nd, Lu-Hf, and 142Nd study of Paleoarchean basalts from the East Pilbara Terrane, Western Australia. Chem. Geol. 578, 120301. Available at: https://doi.org/10.1016/j.chemgeo.2021.120301.

Nutman, A.P., Friend, C.R.L., 2009. New 1:20,000 scale geological maps, synthesis and history of investigation of the Isua supracrustal belt and adjacent orthogneisses, southern West Greenland: a glimpse of Eoarchaean crust formation and orogeny. Precambrian Res. 172, 189–211.

Nutman, A.P., Bennett, V.C., Friend, C.R.L., Rosing, M.T., 1997. ∼ 3710 and ≥ 3790 Ma volcanic sequences in the Isua (Greenland) supracrustal belt; structural and Nd isotope implications. Chem. Geol. 141, 271–287.

Nutman, A.P., Bennett, V.C., Friend, C.R.L., Norman, M.D., 1999. Meta-igneous (non-gneissic) tonalites and quartz-diorites from an extensive ca. 3800 Ma terrain south of the Isua supracrustal belt, southern west Greenland: Constraints on early crust formation. Contrib. Mineral. Petrol. 137, 364–388.

Nutman, A.P., Friend, C.R.L., Bennett, V.C., 2002. Evidence for 3650-3600 Ma assembly of the northern end of the Itsaq Gneiss Complex, Greenland: Implication for early Archaean tectonics. Tectonics 21, 5-1-5–28.

Nutman, A.P., Friend, C.R.L., Bennett, V.C., McGregor, V.R., 2004. Dating of the Ameralik dyke swarms of the Nuuk district, southern West Greenland; Mafic intrusion events starting from c. 3510 Ma. J. Geol. Soc. Lond. 161, 421–430.

Nutman, A.P., Friend, C.R.L., Horie, K., Hidaka, H., 2007. Chapter 3.3 the Itsaq Gneiss complex of Southern West Greenland and the Construction of Eoarchaean Crust at Convergent Plate Boundaries. Dev Precambrian Geol. 15, 187–218.

Nutman, A.P., Bennett, V.C., Friend, C.R.L., Jenner, F., Wan, Y., Liu, D., 2009. Eoarchaean crustal growth in West Greenland (Itsaq Gneiss Complex) and in northeastern China (Anshan area): Review and synthesis. Geol. Soc. Spec. Publ. 318, 127–154.

O'Neil, J., Carlson, R.W., 2017. Building Archean cratons from Hadean mafic crust. Science 355, 1199–1202.

O'Neil, J., Carlson, R.W., Francis, D., Stevenson, R.K., 2008. Neodymium-142 evidence for Hadean Mafic Crust. Science 321, 1828–1832.

O'Neil, J., Rizo, H., Boyet, M., Carlson, R.W., Rosing, M.T., 2016. Geochemistry and Nd isotopic characteristics of Earth's Hadean mantle and primitive crust. Earth Planet. Sci. Lett. 442, 194–205.

O'Neill, H.S.C., Palme, H., 2008. Collisional erosion and the non-chondritic composition of the terrestrial planets. Philos. Trans. R Soc. A Math. Phys. Eng. Sci. 366, 4205–4238.

Palme, H., O'Neill, H., 2013. Cosmochemical Estimates of Mantle Composition, 2nd ed. Elsevier Ltd. Available at. https://doi.org/10.1016/B978-0-08-095975-7.00201-1.

Peters, B.J., Carlson, R.W., Day, J.M.D., Horan, M.F., 2018. Hadean silicate differentiation preserved by anomalous 142Nd/144Nd ratios in the Réunion hotspot source. Nature 555, 89–93.

Pin, C., Zalduegui, J., 1997. Sequential separation of light rare-earth elements, thorium and uranium by miniatureized extraction chromatography: applicaiton to isotopic analyses of silicate rocks. Anal. Chim. Acta 229, 79–89.

Polat, A., Hofmann, A.W., 2003. Alteration and geochemical patterns in the 3.7-3.8 Ga Isua greenstone belt, West Greenland. Precambrian Res. 126, 197–218.

Polat, A., Hofmann, A.W., Rosing, M.T., 2002. Boninite-like volcanic rocks in the 3.7–3.8 Ga Isua greenstone belt, West Greenland : geochemical evidence for intra-oceanic subduction zone processes in the early Earth. Chem. Geol. 184, 231–254.

Polat, A., Frei, R., Fryer, B., Appel, P.W.U., 2009. The origin of geochemical trends and Eoarchean (ca. 3700 Ma) zircons in Mesoarchean (ca. 3075 Ma) ocelli-hosting pillow basalts, Ivisaartoq greenstone belt, SW Greenland: evidence for crustal contamination versus crustal recycling. Chem. Geol. 268, 248–271. Available at: https://doi.org/10.1016/j.chemgeo.2009.09.004.

Polat, A., Frei, R., Scherstén, A., Appel, P.W.U., 2010. New age (ca 2970Ma), mantle source composition and geodynamic constraints on the Archean Fiskenæsset anorthosite complex, SW Greenland. Chem. Geol. 277, 1–20.

Polat, A., Appel, P.W.U., Fryer, B.J., 2011. An overview of the geochemistry of Eoarchean to Mesoarchean ultramafic to mafic volcanic rocks, SW Greenland: Implications for mantle depletion and petrogenetic processes at subduction zones in the early Earth. Gondwana Res. 20, 255–283. Available at: https://doi.org/10.1016/j.gr.2011.01.007.

Puchtel, I.S., Blichert-Toft, J., Touboul, M., Horan, M.F., Walker, R.J., 2016. The coupled 182W-142Nd record of early terrestrial mantle differentiation Igor. Geochemistry Geophys. Geosystems 17, 1312–1338.

Rizo, H., Boyet, M., Blichert-Toft, J., Rosing, M., 2011. Combined Nd and Hf isotope evidence for deep-seated source of Isua lavas. Earth Planet. Sci. Lett. 312, 267–279. Available at: https://doi.org/10.1016/j.epsl.2011.10.014.

Rizo, H., Boyet, M., Blichert-Toft, J., O'Neil, J., Rosing, M.T., Paquette, J.L., 2012. The elusive Hadean enriched reservoir revealed by 142Nd deficits in Isua Archaean rocks. Nature 491, 96–100.

Rizo, H., Boyet, M., Blichert-Toft, J., Rosing, M.T., 2013. Early mantle dynamics inferred from 142Nd variations in Archean rocks from Southwest Greenland. Earth Planet. Sci. Lett. 377–378, 324–335. Available at: https://doi.org/10.1016/j.epsl.2013.07.012.

Rizo, H., Walker, R.J., Carlson, R.W., Touboul, M., Horan, M.F., Puchtel, I.S., Boyet, M., Rosing, M.T., 2016. Early Earth differentiation investigated through 142Nd, 182W, and highly siderophile element abundances in samples from Isua, Greenland. Geochim. Cosmochim. Acta 175, 319–336. Available at: https://doi.org/10.1016/j.gca.2015.12.007.

Rizo, H., Andrault, D., Bennett, N.R., Humayun, M., Brandon, A., Vlastelic, I., Moine, B., Poirier, A., Bouhifd, M.A., Murphy, D.T., 2019. 182W evidence for core-mantle interaction in the source of mantle plumes. Geochemical Perspect. Lett. 6–11.

Rosas, J.C., Korenaga, J., 2018. Rapid crustal growth and efficient crustal recycling in the early Earth: Implications for Hadean and Archean geodynamics. Earth Planet. Sci. Lett. 494, 42–49. Available at: https://doi.org/10.1016/j.epsl.2018.04.051.

Roth, A.S.G., Bourdon, B., Mojzsis, S.J., Touboul, M., Sprung, P., Guitreau, M., Blichert-Toft, J., 2013. Inherited 142Nd anomalies in Eoarchean protoliths. Earth Planet. Sci. Lett. 361, 50–57.

Saji, N.S., Wielandt, D., Paton, C., Bizzarro, M., 2016. Ultra-high-precision Nd-isotope measurements of geological materials by MC-ICPMS. J. Anal. At. Spectrom. 31, 1490–1504.

Saji, N.S., Larsen, K., Wielandt, D., Schiller, M., Costa, M.M., Whitehouse, M.J., Rosing, M.T., Bizzarro, M., 2018. Hadean Geodynamics Inferred from Time-Varying in the Early Earth Rock Record 142 Nd / 144 Nd, pp. 43–48.

Saji, N.S., Wielandt, D., Holst, J.C., Bizzarro, M., 2020. Solar system Nd isotope heterogeneity: Insights into nucleosynthetic components and protoplanetary disk evolution. Geochim. Cosmochim. Acta 281, 135–148. Available at: https://doi.org/10.1016/j.gca.2020.05.006.

Schnabel, C., Muenker, C., Strub, E., 2017. La-Ce isotope measurements by Multicollector-ICPMS. J. Anal. At. Spectrom. 32, 2360–2370. Available at. http://pubs.rsc.org/en/Content/ArticleLanding/2017/JA/C7JA00256D.

Schneider, K.P., Hoffmann, J.E., Boyet, M., Münker, C., Kröner, A., 2018. Coexistence of enriched and modern-like 142Nd signatures in Archean igneous rocks of the eastern Kaapvaal Craton, southern Africa. Earth Planet. Sci. Lett. 487, 54–66. Available at: https://doi.org/10.1016/j.epsl.2018.01.022.

Szilas, K., 2018. A geochemical overview of mid-Archaean metavolcanic rocks from Southwest Greenland. Geosci. 8.

Szilas, K., Hoffmann, J.E., Hansmeier, C., Hollis, J.A., Münker, C., Viehmann, S., Kasper, H.U., 2015a. Sm-Nd and Lu-Hf isotope and trace-element systematics of Mesoarchaean amphibolites, inner Ameralik fjord, southern West Greenland. Mineral. Mag. 79, 857–876.

Szilas, K., Kelemen, P.B., Rosing, M.T., 2015b. The petrogenesis of ultramafic rocks in the >3.7Ga Isua supracrustal belt, southern West Greenland: Geochemical evidence for two distinct magmatic cumulate trends. Gondwana Res. 28, 565–580. Available at: https://doi.org/10.1016/j.gr.2014.07.010.

Szilas, K., Hoffmann, J.E., Schulz, T., Hansmeier, C., Polat, A., Viehmann, S., Kasper, H. U., Münker, C., 2016. Combined bulk-rock Hf- and Nd-isotope compositions of Mesoarchaean metavolcanic rocks from the Ivisaartoq Supracrustal Belt, SW Greenland: Deviations from the mantle array caused by crustal recycling. Chem. Erde 76, 543–554. Available at: https://doi.org/10.1016/j.chemer.2016.09.004.

Thirlwall, M.F., 1991. Long-term reproducibility of multicollector Sr and Nd isotope ratio analysis. Chem. Geol. 94, 85–104. Available at: http://linkinghub.elsevier.com/retrieve/pii/S000925411080021X.

Tusch, J., Sprung, P., van de Löcht, J., Hoffmann, J.E., Boyd, A.J., Rosing, M.T., Münker, C., 2019. Uniform 182W isotope compositions in Eoarchean rocks from the Isua region, SW Greenland: the role of early silicate differentiation and missing late veneer. Geochim. Cosmochim. Acta 257, 284–310.

Tusch, J., Münker, C., Hasenstab, E., Jansen, M., Marien, C.S., Kurzweil, F., Van Kranendonk, M.J., Smithies, R.H., Maier, W.D., Garbe-Schönberg, D., 2021. Convective isolation of Hadean mantle reservoirs through Archean time. PNAS 118, 1–6.

Upadhyay, D., Scherer, E.E., Mezger, K., 2008. Fractionation and mixing of Nd isotopes during thermal ionization mass spectrometry: Implications for high precision 142Nd/144Nd analyses. J. Anal. At. Spectrom. 23, 561–568.

van de Löcht, J., Hoffmann, J.E., Li, C., Wang, Z., Becker, H., Rosing, M.T., Kleinschrodt, R., Münker, C., 2018. Earth's oldest mantle peridotites show entire record of late accretion. Geology 46, 199–202.

van de Löcht, J., Hoffmann, J.E., Rosing, M.T., Sprung, P., Münker, C., 2020. Preservation of Eoarchean mantle processes in ~3.8 Ga peridotite enclaves in the Itsaq Gneiss complex, southern West Greenland. Geochim. Cosmochim. Acta 280, 1–25. Available at: https://doi.org/10.1016/j.gca.2020.03.043.

Vermeesch, P., 2018. IsoplotR: a free and open toolbox for geochronology. Geosci. Front. 9, 1479–1493. Available at: https://doi.org/10.1016/j.gsf.2018.04.001.

Wakaki, S., Tanaka, T., 2012. Stable isotope analysis of Nd by double spike thermal ionization mass spectrometry. Int. J. Mass Spectrom. Ion Process. 323–324, 45–54.

Wang, D., Carlson, R.W., 2022. Tandem-column extraction chromatography for Nd separation: minimizing mass-independent isotope fractionation for ultrahigh-precision Nd isotope-ratio analysis. J. Anal. At. Spectrom. 37, 185–193.

Wilde, S.A., Valley, J.W., Peck, W.H., Graham, C.M., 2001. Evidence from detrital zircons for the existence of continental crust and oceans on the Earth 4.4 Gyr ago. Nature 409, 175–178.

Willbold, M., 2007. Determination of Ce isotopes by TIMS and MC-ICPMS and initiation of a new, homogeneous Ce isotopic reference material. J. Anal. At. Spectrom. 22, 1364–1372.

Wombacher, F., Rehkämper, M., 2003. Investigation of the mass discrimination of multiple collector ICP-MS using neodymium isotopes and the generalised power law. J. Anal. At. Spectrom. 18, 1371–1375.